


Nature and significance of Late Pleistocene to Holocene thick evaporite deposits of the Danakil Depression, Afar, Ethiopia

VALENTIN RIME*[†] , HAILEYESUS NEGGA*[‡], ROBIN FENTIMEN*[§],
ANDRES RÜGGERBERG*, AFIFÉ EL KORH*, CLAUDIUS PIRKENSEER*,
JEAN-CHARLES SCHAEGIS*, IRKA HAJDAS¶, THIERRY ADATTE**,
BALEMWAL ATNAFU‡, TESFAYE KIDANE†† and ANNELEEN FOUBERT*

*Department of Geosciences, University of Fribourg, Ch. Du Musée 6, Fribourg 1700, Switzerland
(E-mail: valentin.rime@unifr.ch)

†School of Geosciences, Faculty of Science, The University of Sydney, Camperdown, Sydney, New South Wales 2050, Australia

‡School of Earth Sciences, Addis Ababa University, 4killo King George VI St, Addis Ababa, Ethiopia
§LPG UMR 6112, Laboratoire de Planétologie et Géosciences, CNRS, Université d'Angers, Nantes Université, Le Mans Université, Angers, France

¶Laboratory of Ion Beam Physics, ETH Zürich, Rämistrasse 101, Zürich 8092, Switzerland

**Faculty of Geosciences and Environment, Lausanne University, Quartier Centre, Lausanne 1015, Switzerland

††Department of Environmental Science and Geology, Wayne State University, 42 W Warren Ave, Detroit, Michigan 48202, USA

Associate Editor – Stephen Lokier

ABSTRACT

Large evaporite deposits, reaching several hundreds of metres of thickness, occur in many basins of our planet but remain poorly understood due to the absence of modern analogues. The origin of ancient evaporites and their highly variable sedimentation rates are often debated and ambiguous. The Danakil rift basin in northern Afar (Ethiopia) features several hundreds of metres of evaporites with deposition still continuing today and, as such, represents a unique modern analogue for older thick evaporite deposits. This study focuses on the multi-proxy analysis of a 625 m long core from the central part of the basin. The core record, dominated by halite (ca 60%) with subordinate clastic sediments (ca 35%) and potash minerals (ca 5%) reveals, for the first time, the Late Pleistocene to Recent geological and environmental history of the basin. Sediments experienced restricted marine conditions after the last Late Pleistocene marine incursion in the basin, followed by a hypersaline stage leading to the near-desiccation of the basin with the deposition of thick halite and potash deposits. Subsequent recycling of marginal halite deposits by meteoric waters in lacustrine and salt pan environments significantly increased the evaporite thickness in the subsiding central part of the basin. These findings have implications for the understanding of older thick evaporite deposits that formed in similar depositional settings. They show that several hundred of metres of evaporite can form in less than 128 kyr by evaporation of meteoric and seawater following a single marine flooding of the basin.

Keywords Bromine, halite, potash, Red Sea, rift, salt giant.

INTRODUCTION

Thick evaporite deposits are present in many sedimentary basins around the world (Hübscher

et al., 2007; Warren, 2010). The thickest and most extensive of those (hundreds to thousands of metres thick and >100,000 km² in area; Rodriguez *et al.*, 2018) are called 'salt giants'. These thick

evaporites remain poorly understood, mainly due to the lack of good modern analogues. In particular, the mechanisms of formation of these evaporites, the hydrological and environmental conditions of these basins, and the surprisingly high sedimentation rates remain ambiguous and debated (e.g. Hsü, 1972; Hübscher *et al.*, 2007; Ryan, 2009; Scribano *et al.*, 2017; Meilijson *et al.*, 2019). The deposition of ancient salt giants may have had profound implications on global seawater salinity, thermohaline oceanic circulation, climate and life evolution (Hay *et al.*, 2006; Shields & Mills, 2020).

The Danakil evaporites, present in the northern part of the Afar Depression (Fig. 1), cover a considerably smaller area than classical salt giants. However, they feature at least 900 m of evaporite-dominated sediments approaching the thickness of known salt giants (Holwerda & Hutchinson, 1968; Warren, 2016). Considering the thickness and Recent age of the Danakil evaporites, they may represent very interesting analogues for some ancient thick evaporite deposits. Understanding and detangling the processes resulting in thick evaporite formation in the Danakil Depression may give insights on the processes that contributed to forming ancient salt giants.

The Danakil evaporites have remained poorly studied due to harsh environmental conditions, challenging accessibility and complex logistics. However, during the last decade, field studies have shed a new light on the sedimentological history of the depression and, in particular, on the Middle to Late Pleistocene Red Sea marine incursions (Atnafu *et al.*, 2015; Foubert *et al.*, 2018, 2024; Jaramillo-Vogel *et al.*, 2019, 2023). In the framework of these studies, industrial data and core material became accessible for research allowing to study the subsurface sediments and evaporites in the central part of the Danakil Depression.

The aim of the present study is to provide a first and general interpretation of the evaporites and adjacent successions in the central part of the basin to better understand: (i) the basin's palaeoenvironmental and hydrological evolution; (ii) the mechanisms of formation of the Danakil evaporites; and (iii) the relevance of the Danakil evaporites for the understanding of other salt deposits from similar depositional settings. Two cores from the basin are studied using a multiproxy approach, including macrofacies and microfacies analysis, sediment component analysis, the study of elemental and mineralogical content, organic matter analysis and absolute dating.

GEOLOGICAL SETTING

The Danakil Depression

The Danakil Depression (Fig. 1A), is part of the Afar Depression, forming a triple junction between the Nubian, Arabian and Somalian plates (Fig. 1B; Rime *et al.*, 2023). The Danakil Depression forms a NNW–SSE oriented rift valley with the lowest point being at 125 m below sea level (Fig. 1A). It is situated between the Ethiopian Plateau reaching more than 3000 m and the Danakil Block where mountains reach >1000 m (Fig. 1A). The counter-clockwise rotation of the Danakil Block (Fig. 1A) relative to Nubia, initiated approximately 10 Myr ago, causing rifting in the Danakil Depression (Eagles *et al.*, 2002; McClusky *et al.*, 2010; Viltres *et al.*, 2020; Rime *et al.*, 2023). In the Danakil Depression, rifting is thought to represent an advanced stage of continental breakup with the Erta Ale volcanic range, possibly marking crustal separation (Barberi *et al.*, 1970, 1972; Barberi & Varet, 1970; Bastow & Keir, 2011; Keir *et al.*, 2013; Le Gall *et al.*, 2018).

Lithostratigraphy

The pre-rift rocks of the Danakil depression comprise a Neoproterozoic basement, unconformably overlain by several clastic and carbonate Palaeozoic and Mesozoic sedimentary units (Fig. 2A; Brinckmann & Kürsten, 1971; Beyth, 1972, 1973, 1978; Varet, 2018). In the early Oligocene, the Traps volcanics, linked to the Afar hotspot, erupted covering most of the region with lava flows (e.g. Mohr & Zanettin, 1988; Ukstins *et al.*, 2002; Coulié *et al.*, 2003; Beccaluva *et al.*, 2009).

The syn-rift sediments of the Danakil Depression are rarely studied with the only basin-wide stratigraphic framework presented by Brinckmann & Kürsten (1971) and the C.N.R. – C.N.R.S. Afar Team (1973). The earliest continental syn-rift sediments of the Danakil Depression are the Late Miocene to Pliocene/Pleistocene *Red Bed Series* or *Danakil Formation* (Brinckmann & Kürsten, 1971; Le Gall *et al.*, 2018; Fig. 2A). They are unconformably overlain by conglomerates interfingering with marine carbonates (Fig. 2A). These marine sediments represent Red Sea incursions that flooded the depression in the Mid to Late Pleistocene. They form mainly fringing coralgal reefs and associated bioclastic and oolitic grainstones, and are named the Zariga Formation

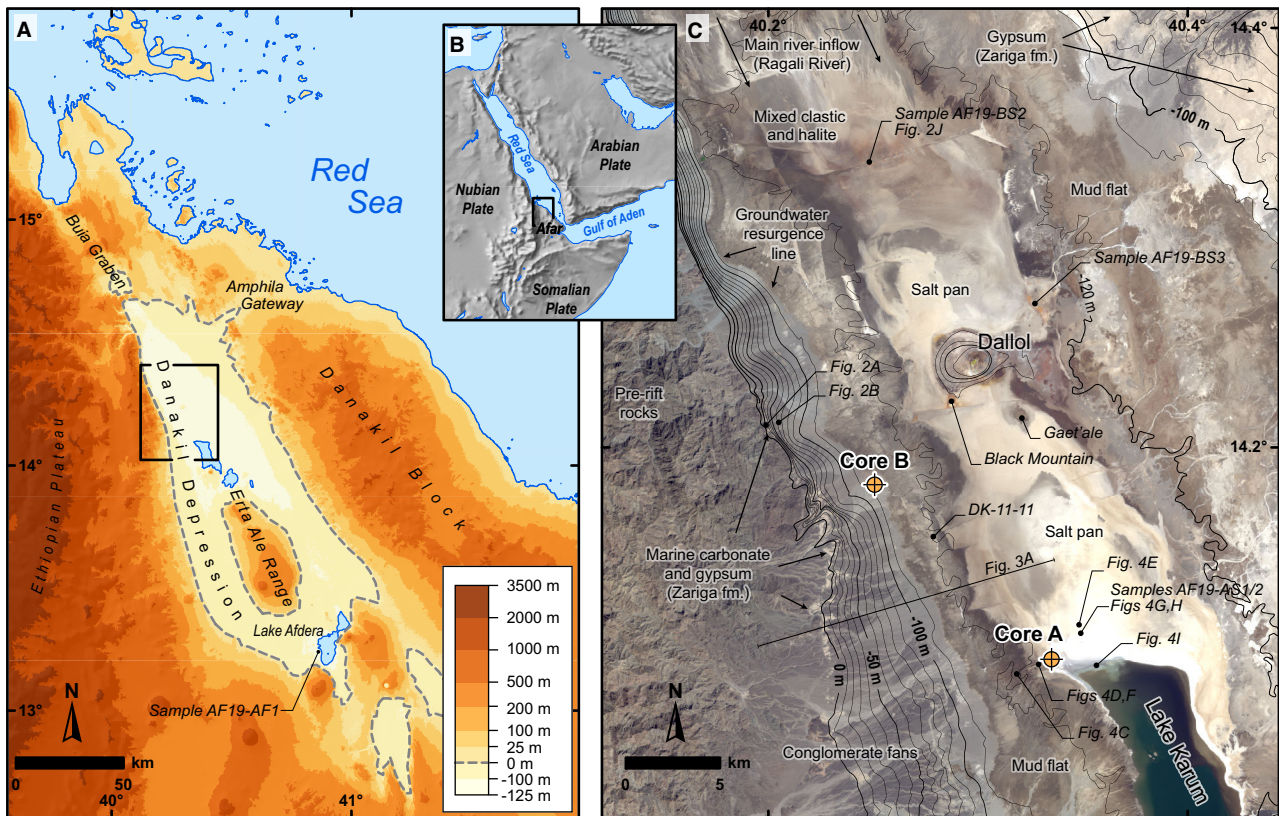


Fig. 1. Maps of the study area. (A) Topographic map of the Danakil Depression. (B) Red Sea and Gulf of Aden region. (C) Landsat 8 image of the salt plain with contours of the topography below sea level from Earth Resources Observation and Science (EROS) Center (2018). Main features and the localization of cores, samples and pictures are indicated.

(Fig. 2A; Faure & Roubet, 1968; Holwerda & Hutchinson, 1968; Lalou *et al.*, 1970; Bonatti *et al.*, 1971; Brinckmann & Kürsten, 1971; Atnafu *et al.*, 2015; Foubert *et al.*, 2018, 2024; Jaramillo-Vogel *et al.*, 2019, 2023). Four different generations of coralgall successions are recognized of which the last two are dated to Marine Isotopic Stage (MIS) 7 and MIS 5e (i.e. *ca* 200 ka and *ca* 128 ka, respectively; Fig. 2A; Foubert *et al.*, 2018; Jaramillo-Vogel *et al.*, 2019; Negga, 2024). The upper (youngest) succession is characterized by a lower open-marine carbonate-rich subunit featuring corals, ooids, echinoderms, bivalves, algae and other marine organisms (Fig. 3B; Brinckmann & Kürsten, 1971; Foubert *et al.*, 2018; Jaramillo-Vogel *et al.*, 2019; Negga, 2024). These deposits are topped by stromatolite-like crusts that laterally correlate with fine (centimetre-scale) alternations of silts and gypsum (Fig. 3B), and represent the transition phase between open marine and restricted hypersaline conditions and the initial isolation

of the Danakil Depression from the Red Sea (Jaramillo-Vogel *et al.*, 2019). The outcrops are overlain by a 10 to 80 cm thick layer of massive gypsum (Fig. 3B; Foubert *et al.*, 2018; Jaramillo-Vogel *et al.*, 2019; Negga, 2024).

The central part of the basin (Fig. 2B) is more poorly known. Based on geophysical data, the sediment thickness south of Dallol (see Fig. 1C for position) is estimated to be between 2.2 km and 3.5 km (Behle *et al.*, 1975; Makris & Ginzburg, 1987). Conversely, Tazieff (1969) and the C.N.R. – C.N.R.S. Afar Team (1973) mention unpublished data showing thicknesses of >4.0 km and 5.5 km, respectively. The deepest well of the depression shows 975 m of “virtually pure, bedded halite” (Holwerda & Hutchinson, 1968). Holwerda & Hutchinson (1968) and Pudovskis *et al.* (2012) mention a possible ‘deep’ potash layer at 930 m in the central part of the basin and at 532 m on the western margin.

However, the vast majority of the scientific and industrial investigations were focused on

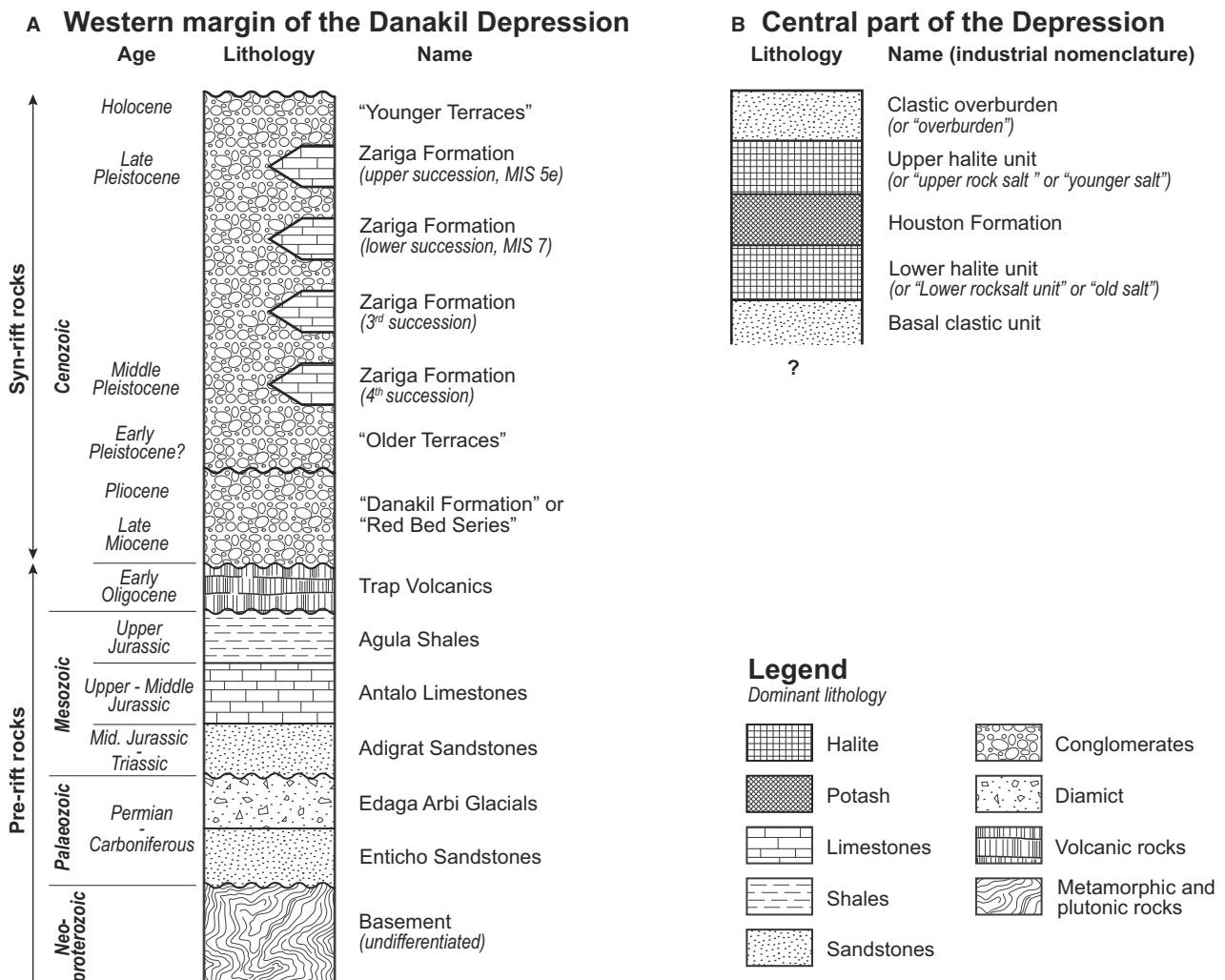


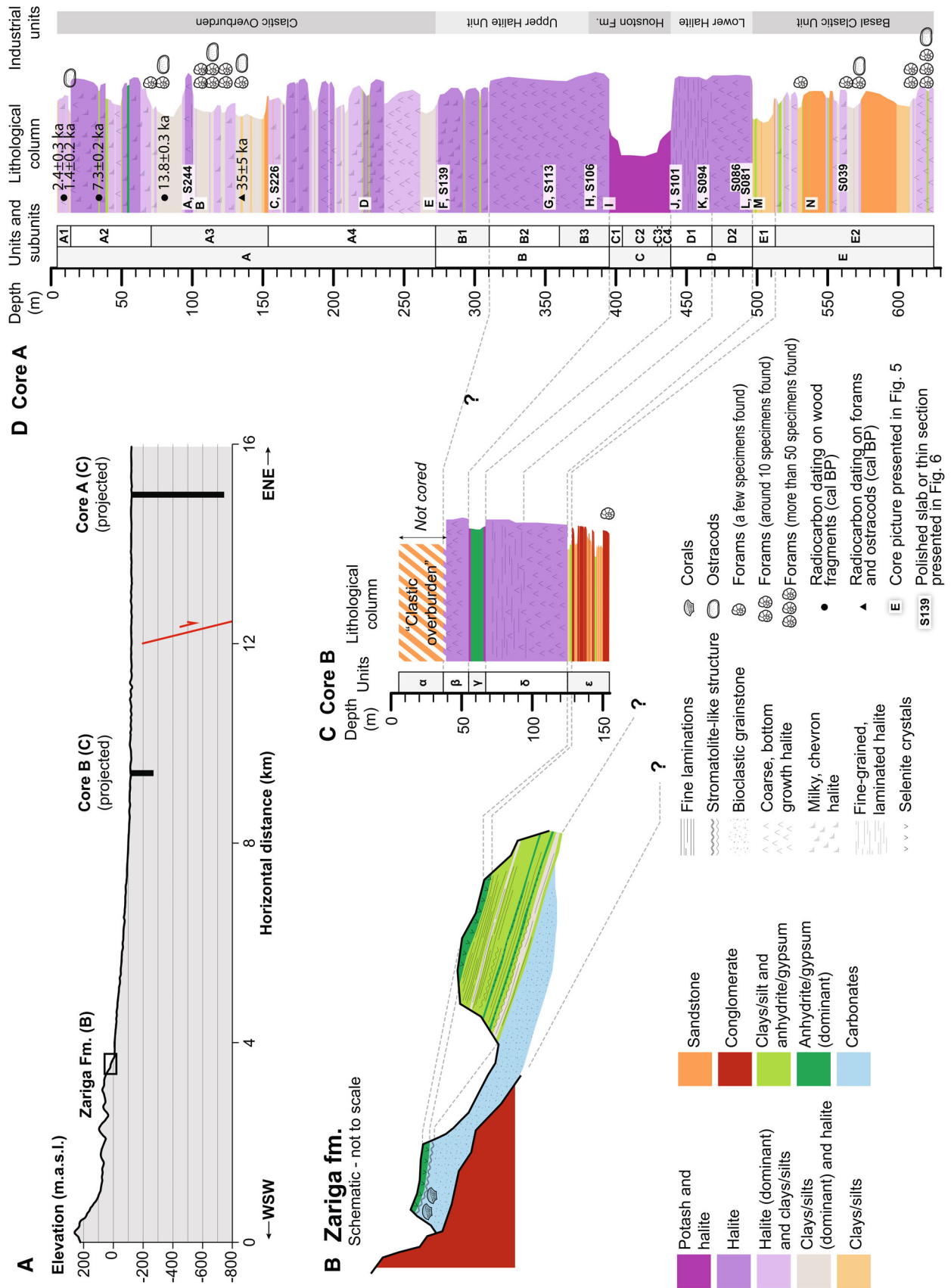
Fig. 2. Simplified lithostratigraphic column of the margin of the Danakil Depression (A) and the central part of the basin (B). After Holwerda & Hutchinson (1968), Brinckmann & Kürsten (1971), Beyth (1972, 1973, 1978), C.N.R. – C.N.R.S. Afar Team (1973), Rauche & van der Klauw (2011), Pudovskis *et al.* (2012), Warren (2016) and Jaramillo-Vogel *et al.* (2019). See text for more information.

the upper part of the sedimentary succession. Based on industrial wells, the following lithostratigraphic units have been identified (Holwerda & Hutchinson, 1968; Hutchinson & Engels, 1972; Rauche & van der Klauw, 2011; Pudovskis *et al.*, 2012; Warren, 2016; Bekele & Schmerold, 2020; Figs 2B and 3D):

1 *Basal clastic unit*: Clastic material ranging from clays to conglomerates.

2 *Lower halite unit (or 'lower rock salt' or 'old salt')*: Halite and occasional seams of anhydrite. Warren (2016) interprets this unit as a shallowing-upward sequence deposited in a subaqueous marine-fed basin.

Fig. 3. Correlation between outcrop and well data of the Danakil Basin. (A) Topographic profile through the depression with the position of cores and outcrops. (B) Conceptual sketch of Late Pleistocene sediments belonging to the Zariga Formation (after Jaramillo-Vogel *et al.*, 2019). (C) and (D) Lithological column of Cores B and A (the width of the column represents the competence of the lithological units, depth represents total core depth). The position of the cores and the cross-section are presented in Fig. 1C. Note that the scale of (B) is approximately 10× that of (C) and (D). Also note that Ca-sulphates in Core A are only found in the form of anhydrite.



3 Houston Formation: This potash unit contains mainly chlorides and K and Mg-rich salts. It is divided into four subunits (from bottom to top): (i) the Kainite Member formed by laminated kainite and halite; (ii) the Intermediate Member composed of mixed and varying mineralogies often featuring a lower carnallite bed, a bischofite bed and an upper carnallite bed; (iii) the Sylvite Member, rich in sylvite, polyhalite, anhydrite and halite; (iv) the Marker Beds formed by bedded halite with wavy anhydrite seams and clays. Holwerda & Hutchinson (1968) interpret the Houston Formation as the primary deposition of a lower kainite bed overlain by a carnallite-rich bed that was leached in its upper part, removing MgCl_2 to form the Sylvite Member. Warren (2016) also interprets the Kainite Member as a primary, sub-aqueous, depositional unit formed by the evaporation of seawater. Conversely, the Intermediate Member is interpreted to have experienced significant alteration and early diagenesis by shallow phreatic brines, possibly formed during the instalment of a freshened brine lake or seaway. The Sylvite Member is also interpreted as a recrystallized unit, possibly of a carnallite precursor, containing barren zones of halite indicating the inflow of fresher waters.

4 Upper halite unit (or 'upper rock salt' or 'younger salt'): Medium to coarse-grained, bottom-nucleated poorly bedded halite with microkarst textures, variable anhydrite and clastic content, the latter increasing upward. Warren (2016) interprets this unit as corresponding to a freshening upward cycle developed in a saline pan with meteoric water influence.

5 Clastic overburden (or 'overburden'): Alluvial gravels, fine siliciclastic material, and intercalated beds of gypsum and halite. While some cores have a sharp contact between the *clastic overburden* and the *upper halite unit*, others show a more gradual transition (Holwerda & Hutchinson, 1968). This unit is often poorly described because it was rarely cored. It was described to thicken towards the western margin of the depression (Holwerda & Hutchinson, 1968).

Overall, the mechanisms of formation of the evaporites in the central part of the basin are still debatable, as well as their age, timespan of deposition and their correlation with outcrops at the margins of the basin. Based on faunal evidence, Holwerda & Hutchinson (1968) propose a mid or late Quaternary age for sediments situated above the potash unit. Brinckmann & Kürsten (1971) hypothesize Pliocene to Quaternary ages. Hutchinson & Engels (1970) reports K/Ar dating on sylvite (Houston Formation) with ages ranging between 76 and 88 ka \pm 15%. The C.N.R. – C.N.R.S. Afar Team (1973) mention an additional K/Ar dating on salt of 125 ka. However, the diagenetic nature of the sylvite deposits in the Danakil Depression (see above) and the known low reliability of this dating technique on sylvite (Hurley, 1966; Brookins *et al.*, 1980) strongly question these results. Due to similarities with Red Sea evaporites, some authors even hypothesized that the lower evaporites might be Miocene in age (Talbot, 2008; López-García *et al.*, 2020).

Climate and Recent sedimentation

Climate

The Danakil Depression is considered a hot desert according to the Köppen climate classification (Fazzini *et al.*, 2015). It holds the record for the highest annual mean temperature with 34.4°C measured between 1960 and 1966 (Cerveny *et al.*, 2007) and temperatures above 50°C have been measured during summer (Cavalazzi *et al.*, 2019). The depression experiences less than 200 mm of precipitation per year (Fazzini *et al.*, 2015). Higher precipitation rates are noted on the escarpment and the neighbouring Ethiopian plateau (>500 mm/year in Mekele; Fazzini *et al.*, 2015).

Present-day geological processes in the Danakil Depression

Rivers are eroding the basement and Mesozoic sediments around the margins of the depression (Brinckmann & Kürsten, 1971; Rime *et al.*, 2022;

Fig. 4. Present-day sedimentary facies in the Danakil Depression. The approximate position of each picture is presented in Fig. 1C. (A) Fluvial channel cutting through older sediments. The salt plain and Dallol volcano can be recognized in the far distance. (B) Sheetflood event transporting clastic material into the basin (C) saline mudflat. (D) Salt flat with polygonal structures. (E) Halite rafts forming in a karstic pool at the surface of the salt plain. (F) Recent rafts deposited on the salt flat during the last flooding. (G) Euhedral halite crystals. Note that these crystals were found approximately 5 to 10 cm below the surface. (H) Uppermost layer of the salt flat. White arrows point towards chevron halite crystals. (I) Cold spring feeding Lake Karum. (J) Unusual, red-coloured pond on the salt flat.

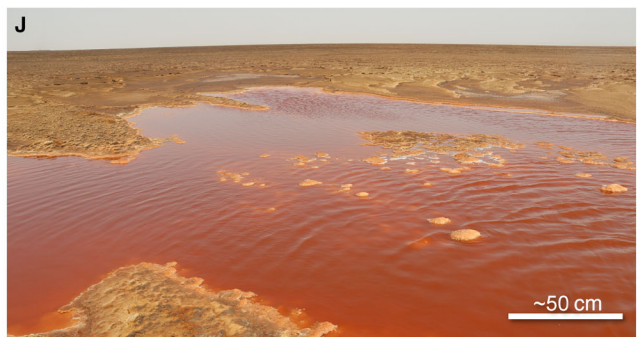
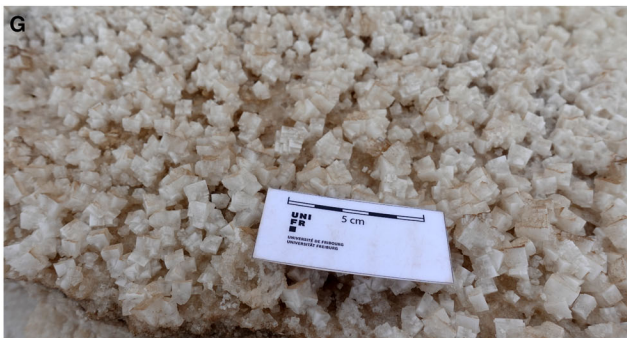
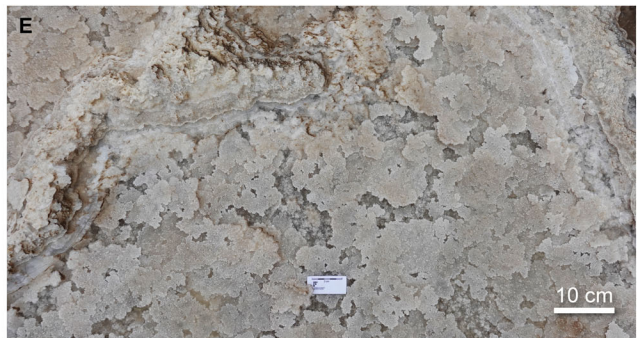
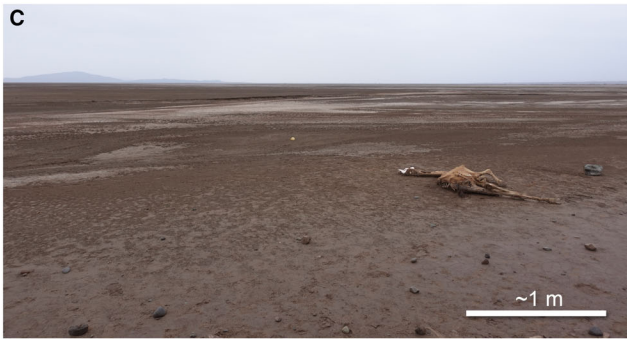
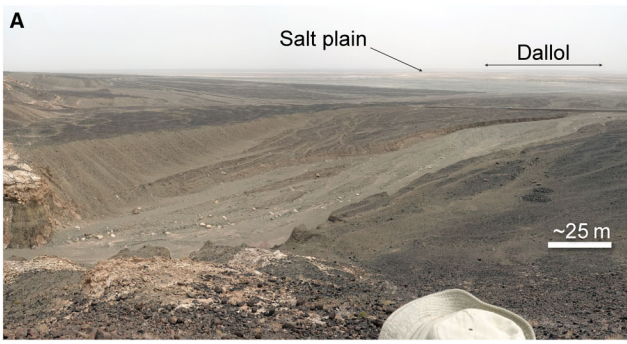


Fig. 4A). Sheetfloods, caused by seasonal sporadic precipitation events on the escarpments (Fig. 4B), result in the deposition of conglomerates with up to metre-sized boulders on the margins of the depression. Grain size decreases distally, with silt and mud-sized particles forming a mud flat (Figs 1C and 4C). The facies then gradually evolves towards the central part of the depression into a >5 km wide saline pan characterized by metre-sized halite polygons in the central part of the depression (Figs 1C and 4D). Artisanal mining of this halite has been known for centuries (Munzinger, 1869) and was still ongoing in 2020. Halite is formed each year during flooding of the salt plain by ephemeral and very shallow lakes (López-García *et al.*, 2020). Halite rafts and hopper crystals (Fig. 4E and F) form at the water–air interface by evaporation and sink to the lake floor. On the lake floor, halite grows as syntaxial overgrowths on settled rafts and hoppers, forming cubic halite beds and crusts (Fig. 4G). With time, halite crusts and darker laminae representing impurities due to fluvial or aeolian input form the uppermost sediment fill of the basin (Fig. 4H). During dry periods, the water table is situated only a few (tens of) centimetres below the surface with only Lake Karum (Fig. 4I, see Fig. 1C for position) remaining flooded throughout the year. Due to the very arid climate in the depression, most of the water present in the depression drains from the escarpments. Rivers flowing through pre-rift basement and sediments on the escarpment have low salinities (Kebede *et al.*, 2008; Meaza *et al.*, 2019). These rivers mostly disappear from the surface at the margins of the depression and flow through the subsurface into the depression where their measured salinity increases drastically (Ralph M. Parsons Company, 1967), indicating dissolution of ancient evaporites. They then resurge at the lowest part of the depression (Fig. 1C) or as saline springs such as in Lake Karum (Fig. 4I).

Dallol volcano and hot springs

The basin is also characterized by the Dallol salt volcano and surrounding hot springs that are found in its central part (see Fig. 1C; Holwerda & Hutchinson, 1968; Talbot, 2008; Nobile *et al.*, 2012; Master, 2016; Warren, 2016; Cavalazzi *et al.*, 2019; Kotopoulou *et al.*, 2019; López-García *et al.*, 2020; Otálora *et al.*, 2022). Magmatic intrusions are believed to have caused dehydration and hydrolysis of evaporite minerals, the doming of the evaporites and hydrothermal activity at the surface (Otálora *et al.*, 2022). Talbot (2008) proposes that

the dome is mainly formed by marine salts: “with minor local additions of hydrothermal salts”. The *Black Mountain*, situated south-west of Dallol (Fig. 1C), is a hot spring with MgCl₂-rich fluids crystallizing bischofite and carnallite (Holwerda & Hutchinson, 1968; Kotopoulou *et al.*, 2019; López-García *et al.*, 2020). One of its ponds, *Black Lake*, is probably the most saline body in the world (>70%, Belilla *et al.*, 2019). Similarly, *Gaet'ale Pond* (also called *Yellow Lake*) is extremely saline, dominated by CaCl₂ and MgCl₂ salts (Pérez & Chebude, 2017; Kotopoulou *et al.*, 2019) and producing carnallite deposits (López-García *et al.*, 2020). These hot springs and their related evaporitic deposits are spatially very restricted and do not contribute significantly to the stratigraphy of the basin (Holwerda & Hutchinson, 1968; Talbot, 2008; López-García *et al.*, 2020).

MATERIAL AND METHODS

Two cores were studied and sampled, Core A [drilled by BHP Billiton, industry name: DAN0003D, 14.0986N, 40.3349E, 120 m.b.s.l. (metres below sea level), Figs 1C, 3A and 3C] and Core B (drilled by Allana Potash Corp., industry name: DK-11-14, 14.182N, 40.2506E, 116 m.b.s.l., Figs 1C, 3A and 3B). Core A is the only available deep (625 m) borehole in the basin cored throughout its entire length and reaching sediments below the *Lower Halite Unit*. This core is situated in the central part of the basin (Figs 1C and 3A) and unpublished seismic reflection data (Pudovskis *et al.*, 2012) do not show major unconformities over the cored interval, indicating a continuous sedimentary record. For those reasons, Core A was identified as the reference core within the framework of this study. In total, 277 bulk rock samples were taken from the core at regular depth intervals and representing the different sedimentary facies. Samples were analysed for sedimentary petrography, sediment component analyses (microfauna), geochemistry [total organic carbon (TOC) and X-ray fluorescence (XRF)], dating (¹⁴C) and mineralogical analyses (X-ray diffraction – XRD) resulting in more than 600 measurements (Table S1). Core B is 155 m long with coring starting at 39 m. Core B was drilled in a more marginal position of the basin (Figs 1C and 3A), west of the major fault system forming the central graben (Bastow *et al.*, 2018). Due to sample restrictions, only thirteen samples were available for microfauna analyses. Five additional evaporite samples representing evaporites of both relatively large

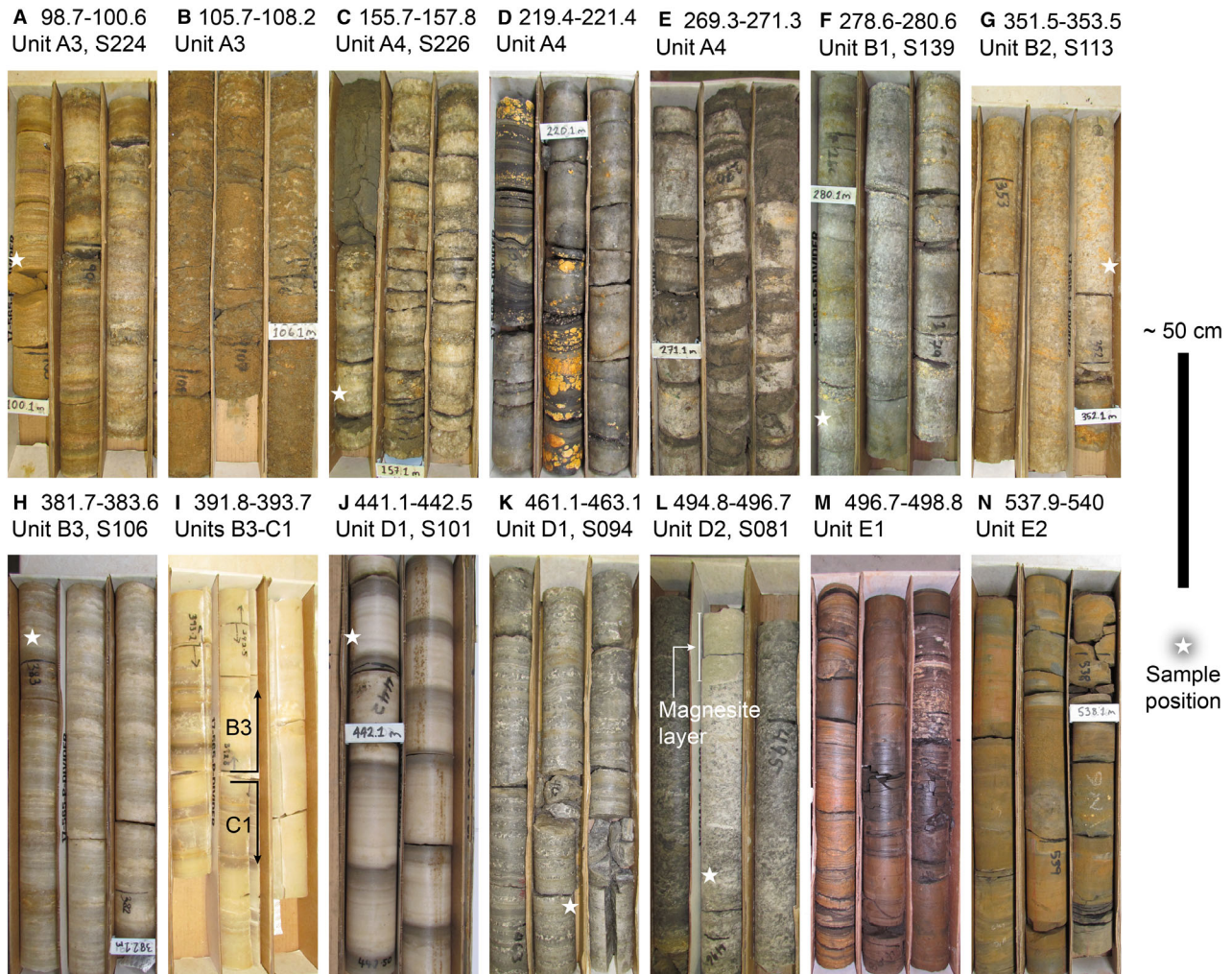


Fig. 5. Pictures of Core A. Position of the pictures on Fig. 3D. Depth (in m), unit and sample numbers presented on Fig. 6 are indicated. (A) Laminated medium to fine-grained halite. (B) Clays and silts with foraminifera and intra-sediment halite. (C) Alternation of cloudy halite and clastic sediments. (D) Clays and anhydrite between two halite layers. (E) Silt and halite alternations. (F) Cloudy halite alternating with anhydrite layers. (G) Coarse halite. (H) Laminated but coarse halite, with dissolution surfaces. (I) Conformable transition between unit C1 (carnallite, banded) and unit B3 (halite). (J) Fine-grained, laminated halite. (K) Alternation of fine-grained, laminated halite and coarse halite. (L) Coarse halite forming the lowermost part of unit B. The greenish magnesite layer is visible. (M) Clayey unit forming the uppermost part of unit A. (N) Sand layer.

lakes and smaller ponds were taken at the surface of the depression (Fig. 1A and C; Table S1) for elemental and mineralogical analysis.

Facies analysis

Facies analysis of Core A is based on the macroscopic description of full and half core sections (Fig. 5), unpublished geological descriptions by BHPB in Pudovskis *et al.* (2012), and the petrographic study of core slabs and thin sections (Fig. 6). Halite and other consolidated sediments

were cut dry from half core sections as 5 to 10 cm slabs with a circular saw mounted with a diamond blade. For thin section preparation, the slabs were further cut with a dry diamond wire saw. Petrographic thin sections were prepared at the Department of Geosciences of the University of Fribourg using a diamond polishing pad lubricated with petrol to avoid dissolution.

The facies of Core B was described based on visual inspection of half and full core sections, combined with the analyses of core pictures. In the case of non-recovery, downhole logging data

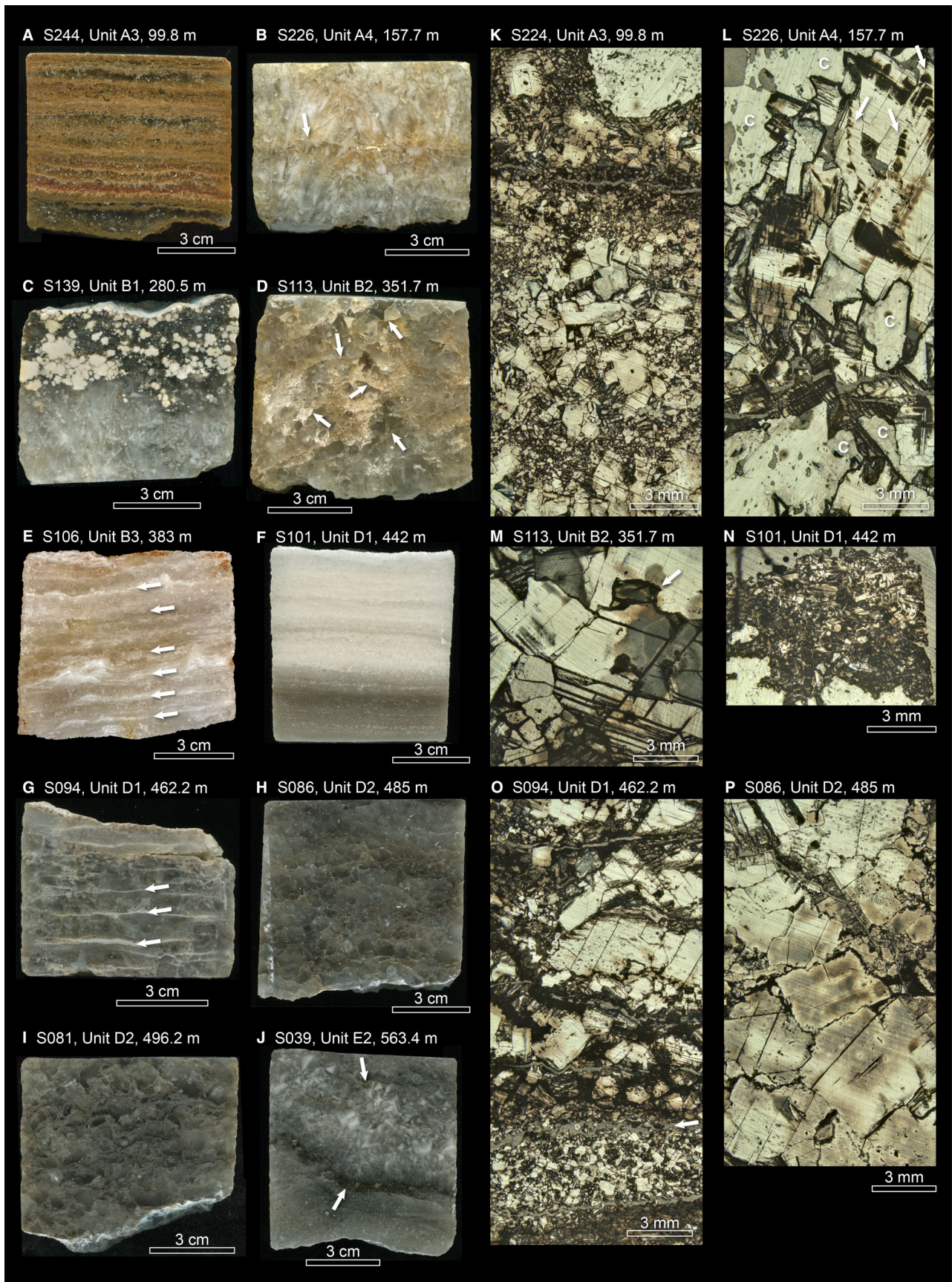


Fig. 6. Macrofacies (A) to (J) and microfacies (K) to (P) of evaporites. Sample number, unit and depth are indicated. The position of the samples is also indicated on Figs 3D and 5. (A) and (K) Fine to medium-grained laminated fabric. (B), (C), (J) and (L) Cloudy chevron halite. Arrows on (B) and (J) indicate dissolution surfaces. Arrows on (L) show inclusions highlighting the chevron structure. 'C' shows clear halite cement in cavities. (D), (E) and (M) Coarse-grained, bottom growth halite with dissolution surfaces (arrows). (F) and (N) Fine-grained, laminated halite. (G) and (O) Laminated alternations between coarse-grained and fine-grained halite. The white arrows represent polyhalite layers measured in X-ray diffraction (XRD) but removed during thin section preparation. (H), (I) and (P) Coarse-grained, bottom growth halite with dissolution features around the individual crystals. (J) Cloudy chevron halite with dissolution surfaces (white arrows).

(Rauche & van der Klauw, 2011) were used to refine facies descriptions.

Non-evaporitic sediments were described according to grain size (clay, silt, sand and gravel). Evaporites are described on the basis of their main mineralogy (sulphates, potash and halite) and halite texture (clear, medium to coarse-grained bottom-growth halite; cloudy chevron halite and laminated, fine-grained halite). Note that the term potash is used here in its broadest sense, including all high-concentration evaporite minerals and not only K-rich varieties.

Sediment component analysis

Samples of clastic sediments were wet sieved at 1 mm, 125 μm , 63 μm and 32 μm (51 samples from Core A and 13 from Core B). The 63 μm and 125 μm fractions were hand-picked for qualitative microfaunal analyses. Relevant specimens were photographed and identified using standard optical microscopy (Nikon SMZ18; Nikon, Tokyo, Japan) and scanning electron microscopy (Thermo Fischer SEM FEIXL30SFEG – Thermo Fisher Scientific, Waltham, MA, USA; Department of Geosciences, University of Fribourg).

Geochemistry

In total, 179 samples were analysed for elemental content by wavelength dispersive X-ray fluorescence (WD-XRF) using a PANalytical Zetium XRF spectrometer (Malvern Panalytical, Malvern, UK; Department of Geosciences, University of Fribourg) (see Table S1). Bulk clastic and evaporite (halite) samples were prepared as pressed pellets (12 g of sample + 3 g of wax). Evaporite samples were first prepared according to Herrmann *et al.* (1973) and Moretto (1988). Samples were crushed in ethanol, generously rinsed with ethanol and filtered to avoid fluid inclusion signals. Clastic samples were analysed for major and trace elements using the semi-quantitative Omnia and

quantitative ProTrace calibrations, and applications developed by Malvern PANalytical. Major elements, Cl and Br in halite samples were quantitatively measured using a specific calibration running on the Super-Q software and based on 22 in-house prepared pressed pellet standards composed of a mixture of halite, KBr, anhydrite and silicates. Measurement of a short series of trace elements (Sr, Ba) was performed using the ProTrace calibration. These calibrations have a relative uncertainty of 1% for the major elements and 10% for the minor elements (Morel & Serneels, 2021; Nitsche *et al.*, 2023; Rodier & Serneels, 2023). Detection limits are given by the software and presented in the figures and in Table S1.

In order to confirm the bromine measurements, independent ion chromatography (IC) analyses were conducted using a Dionex™ ICS-2100 (Thermo Scientific™) equipped with Dionex™ IonPac™ AS30 analytical and guard columns at the Department of Geosciences, University of Fribourg, Switzerland. The results of these measurements are reported in Supporting Document S1. They correlate well with XRF data ($R^2 = 0.9968$) but led to small systematic correction of the XRF data. These results show a relative uncertainty lower than 9% for the presented bromine values (see Supporting Document S1).

Bromine content in halite is a proxy for brine parenthood and ion concentration (Boeke, 1908; Valyashko, 1956; Raup & Hite, 1978). As an incompatible element in halite, its abundance in crystals will rise with increasing ion concentration of the brine (e.g. McCaffrey *et al.*, 1987). Conversely, the recycling of marine evaporites by meteoric water will produce halite with lower bromine content (Holser, 1979; Warren, 2016).

There is a long history of controversy about the bromine content of the first halite precipitating from marine water and, thus, the potential use of bromine as a proxy for distinguishing marine and meteoric parent fluids. While the theoretical

minimum Br content should be 60 to 75 ppm in marine waters (Holser, 1966; Herrmann, 1972; Herrmann *et al.*, 1973), it has been shown that Br partition coefficient varies according to crystal growth rates, chemical composition of the brines (especially MgCl_2 content) and, to a small degree, temperature (Braitsch & Herrmann, 1963; Holser, 1966; Herrmann, 1972, 1980; Herrmann *et al.*, 1973).

Generally, the threshold values of the Br-content between marine and meteoric fluids varies between 40 and 75 ppm (e.g. Valyashko, 1956; Kuhn, 1968; Herrmann *et al.*, 1973; Kühn & Hsü, 1974; Holser, 1979; Holland, 1984; Wilgus & Holser, 1984; McCaffrey *et al.*, 1987; Garcia-Veigas *et al.*, 1995; Raup & Hite, 1996; Schreiber & El Tabakh, 2000; Cendón *et al.*, 2004; Brennan *et al.*, 2013; Warren, 2016; Blamey & Brand, 2019; Ercan *et al.*, 2019; Karakaya *et al.*, 2019).

As pointed out by Hardie (1984), Taberner *et al.* (2000), Babel & Schreiber (2014) and Warren (2016), the identification of marine versus meteoric parent brines should therefore not only rely on bromine content but also on additional stratigraphic, sedimentological, mineralogical and geochemical evidence.

Additional geochemical analyses from BHPB and Allana Potash Corp. were used for refining the facies descriptions of the potash interval of Cores A and B (Figs S1 and S2). Geochemical analyses on Core A were performed by BHPB using a hand-held XRF [Innov-X Delta model (Olympus, Tokyo, Japan) used in Mining Plus mode; Pudovskis *et al.*, 2012]. Geochemical analyses on Core B were performed by Kali-Umwelttechnik GmbH (Sondershausen, Germany) for Allana Potash Corp. by flame emission spectrometry (K^+ , Na^+ , Mg^{2+} , Ca^{2+}) and ion chromatography (Cl^- , SO_4^{2-}) and were reported by Rauche & van der Klauw (2011).

Organic matter analyses of 25 samples from the clastic fraction were performed with Technologies Vinci Rock-Eval 6 at the Institute of Earth Sciences of the University of Lausanne. Total organic carbon (TOC, wt%), hydrogen index (HI, mg HC/g TOC, HC = hydrocarbons) and oxygen index (OI, mg CO_2 /g TOC) were measured (see Table S1). The HI and OI give an indication of the origin of the organic matter (e.g. Van Krevelen, 1993).

Mineralogy

In total, 186 mineralogical analyses on bulk samples (hand-crushed in agate mortar) were

performed with the Rigaku Ultima IV X-ray diffractometer (XRD; Rigaku, Tokyo, Japan) at the Department of Geosciences, University of Fribourg. The samples were measured from 15° to 70° 2θ at $1.3^\circ/\text{min}$ (step size 0.02°) with an X-ray source (Cu-anode, LFF) operating at 40 kW, 40A and a D/teX Ultra detector. The results were analysed with the Rigaku PDXL2 software, using the Rietveld method for a semi-quantitative analysis of clastic samples. In Fig. 7, phyllosilicates, as well as Ca-carbonates (calcite and high-Mg calcite) are grouped. Quantities are normalized to 100%, excluding evaporite minerals.

Radiocarbon dating

Radiocarbon dating was performed on small wood fragments, as well as on foraminiferal tests, ostracod carapaces and other skeletal fragments. Organic matter such as wood was treated to remove contamination by carbonates and humic acids. This was done by washing samples with an acid and a base at 60°C for 1 h each step (0.5 M HCl, 0.1 M NaOH, 0.5 M HCl, washes with MilliQ water in between) (Hajdas, 2008).

Dry sample material was weighed within aluminium cups for combustion in the Elemental Analyser. Skeletal material was dissolved in concentrated phosphoric acid. The CO_2 was analysed using a Gas Ion Source (GIS) at the MICADAS system at ETH Zürich (Synal *et al.*, 2007). Radiocarbon ages were calibrated using OxCal 4.4.4 and the IntCal20 calibration curve (Reimer *et al.*, 2020; see Fig. S3). The ages of the foraminifera and marine skeletal material were close to the limit of radiocarbon dating. No reservoir correction was applied because it is unknown.

RESULTS

Sedimentary petrography

Core A

Core A has been divided into five major units and 15 subunits based on facies variations, mineralogy, elemental content and faunal analyses (Fig. 3). Core A is composed of *ca* 67% of evaporites (*ca* 60% halite, *ca* 6% potash and *ca* 1% anhydrite). Sulphates are only present as anhydrite and not as gypsum in the core. Besides evaporites, 33% of the core is composed of siliciclastic and carbonate sediments. Their grain size ranges from clay to sand. Dominant mineralogical assemblages in the non-evaporitic samples

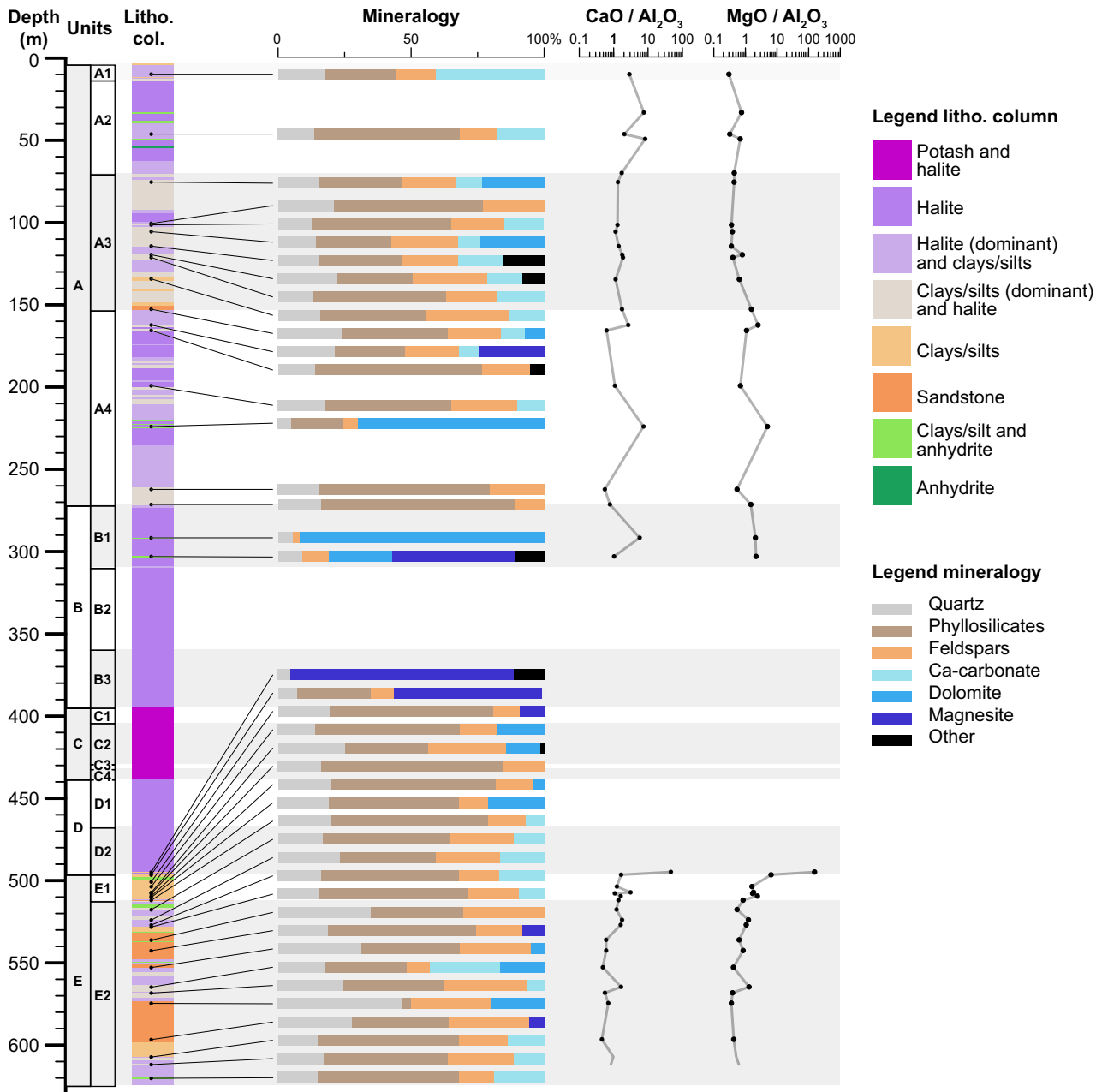


Fig. 7. Mineralogical and elemental content of bulk non-evaporitic samples of Core A. Mineralogy from semi-quantitative X-ray diffraction (XRD) analysis, normalization excluding evaporite minerals. X-ray fluorescence (XRF) data show $\text{CaO}/\text{Al}_2\text{O}_3$, and $\text{MgO}/\text{Al}_2\text{O}_3$ ratio.

are phyllosilicates, quartz and feldspars, while carbonates are composed of Ca-carbonates, dolomite and magnesite. These assemblages mainly reflect the composition of sedimentary grains and/or the bioclastic content. Some layers are more enriched in dolomite and magnesite representing chemical precipitates and/or diagenetic minerals. Sediment component analysis revealed the presence of foraminifera, diatoms, ostracods and skeletal

fragments. Overall, the siliciclastic fraction dominates the non-evaporite part of the core (Fig. 7), which will be called ‘clastics’ hereafter.

Unit E (625.1 to 496.7 m) is dominated by clastics (ca 70%). Subunit E2 mainly comprises an alternation between halite (ca 30%) and clastics (ca 70%, with variable amounts of calcite). Clastic units are clay to sand grade (Fig. 5N) and mainly composed of quartz and phyllosilicates with

minor amounts of carbonates and feldspars (Fig. 7). Minor anhydrite layers (*ca* 2%) are present. Subunit E2 is characterized by the presence of foraminifera [*Ammonia veneta* (over 50% relative abundance), *Quinqueloculina semiluna*, *Triloculina oblonga*, *Brizalina striatula*, *Bulimina elongata* and *Rosalina globularis*; Figs S4 and S5] and ostracods (*Cyprideis*; Fig. S6). Subunit E1 (Fig. 5M) is formed by silty to clay-rich material, mainly composed of phyllosilicates. Dolomite and magnesite (pure Mg-carbonate) are dominantly present at the top of the subunit (Fig. 7).

Unit D (496.7 to 438.83 m) is composed exclusively of evaporites. While dominated by halite, XRF and XRD data (Fig. 8) indicate the presence of anhydrite, polyhalite and possibly kieserite in unit D. Subunit D2 shows clear, coarse-grained bottom growth halite (Figs 5L, 6H and 6I). At the base of the unit, XRD data shows a 10 cm interval (Fig. 5L) of magnesite, anhydrite and huntite (Fig. 7). Subunit D1 shows the transition from alternations (between 1 cm and 6 cm thick) of fine-grained and coarse-grained halite at the base (Figs 5K, 6G and 6O) to fine-grained, laminated halite (Figs 5J and 6F) with cubic crystals (Fig. 6N) in the upper part of the subunit. The upper fine-grained laminated halite is characterized by cyclic changes in colours (between 1 cm and 25 cm thick; Fig. 5J).

Unit C (438.83 to 395.3 m) is formed entirely by potash minerals, complex salts and halite. Based on facies analyses and portable XRF data, Pudovskis *et al.* (2012) recognize four mineralogical assemblages in unit C (see Fig. S1 for XRF data). Subunit C4 shows high sylvite content (with K₂O reaching 50%) along with carnallite and kainite. Subunit C3 shows mainly kainite with millimetre to centimetre-scale laminations/bedding. Subunit C2 shows bischofite with kainite bands forming irregular cycles between 1 cm and 30 cm. Subunit C1 shows a mix of carnallite, polyhalite, kainite and possibly kieserite forming beds between 1 cm and 25 cm thick.

Unit B (395.3 to 272.3 m) is composed almost entirely of halite (*ca* 95%), except for the presence of minor anhydrite (3%) in subunits B3 and B1, exclusively and some clastic material (10%) in subunit B1. The facies at the base of subunit B3 shows medium-grained, clear halite (Fig. 5I). Up-section, it changes to coarse clear halite with frequent (approximately each centimetre) dissolution horizons and colour change, resulting in laminations (Figs 5H and 6E). At the top of the subunit, these dissolution surfaces disappear, only showing (very) coarse (centimetre-scale)

clear halite. Subunit B2 is composed exclusively of coarse clear halite (Figs 5G and 6D). Subunit B1 mainly shows a cloudy chevron texture with some intercalations of anhydrite (Figs 5F and 6C) and minor intervals enriched in dolomite and magnesite (Fig. 7).

Unit A (272.3 to 4.3 m) is mainly composed of an alternation of halite (*ca* 60%) and clastic material (*ca* 40%) (Figs 3D and 5). Subunit A4 shows an alternation of clastic (*ca* 60%) and evaporitic (*ca* 40%) material (Figs 3D and 5C to E). Halite is either found as interstitial displacive halite within clastic sediments or is present as clear, coarse, bottom-growth halite, or as cloudy, chevron halite with dissolution surfaces and clear halite cements in millimetre to centimetre-scale cavities (Fig. 6B and L). Some clastic intervals show nodular and chicken-wire anhydrite (Fig. 5D), sometimes associated with dolomite (Fig. 7). Subunit A3 is dominated by clastic material (*ca* 70%; Fig. 5B). The lower 2.5 m of this subunit is marked by sandstone but the rest of the subunit is composed of silt to clay material. Two intervals (at *ca* 95 m and *ca* 120 m) show a higher halite content (Figs 3D, 5A, 6A and 6K). The facies are either cloudy, with millimetre to centimetre-scale alternations of fine-grained and coarser halite (Fig. 6A and 6K) or clear coarse-grained halite. Subunit A2 presents two intervals nearly devoid of clastic material (14 to 39 m, 50 to 63 m) separating a more clastic-rich interval (39 to 50 m). Most of the halite presents a cloudy texture. Subunit A1 is formed by clastics (*ca* 60%) with frequent displacive halite or as halite beds (*ca* 40%).

Subunits A3 and the base of A2 show the presence of microfauna (Fig. 3D). This fauna is more diverse than in unit E2 with a total number of 11 identified foraminifera species. *Ammonia veneta* is also the dominant species, whilst minor species are essentially represented by *Quinqueloculina* spp. (*Q. semiluna* and *Q. viennensis*), *Elphidium* spp. (*E. williamsoni* and *E. advenum*), *Bulimina elongata*, *Bolivina pseudoplicata*, *Nonion fabum* and *Haynesina depressula* (Figs S4 and S5). Ostracod species belong to the genera *Cyprideis* and *Loxoconcha* (Fig. S6).

The top 4.3 m of the borehole were not recovered.

Core B

Core B is divided into five units (see Figs 3B and S2). Because of significant differences in mineralogy and facies between Cores A and B, different unit names are used (Greek letters for Core B versus Latin letters for Core A).

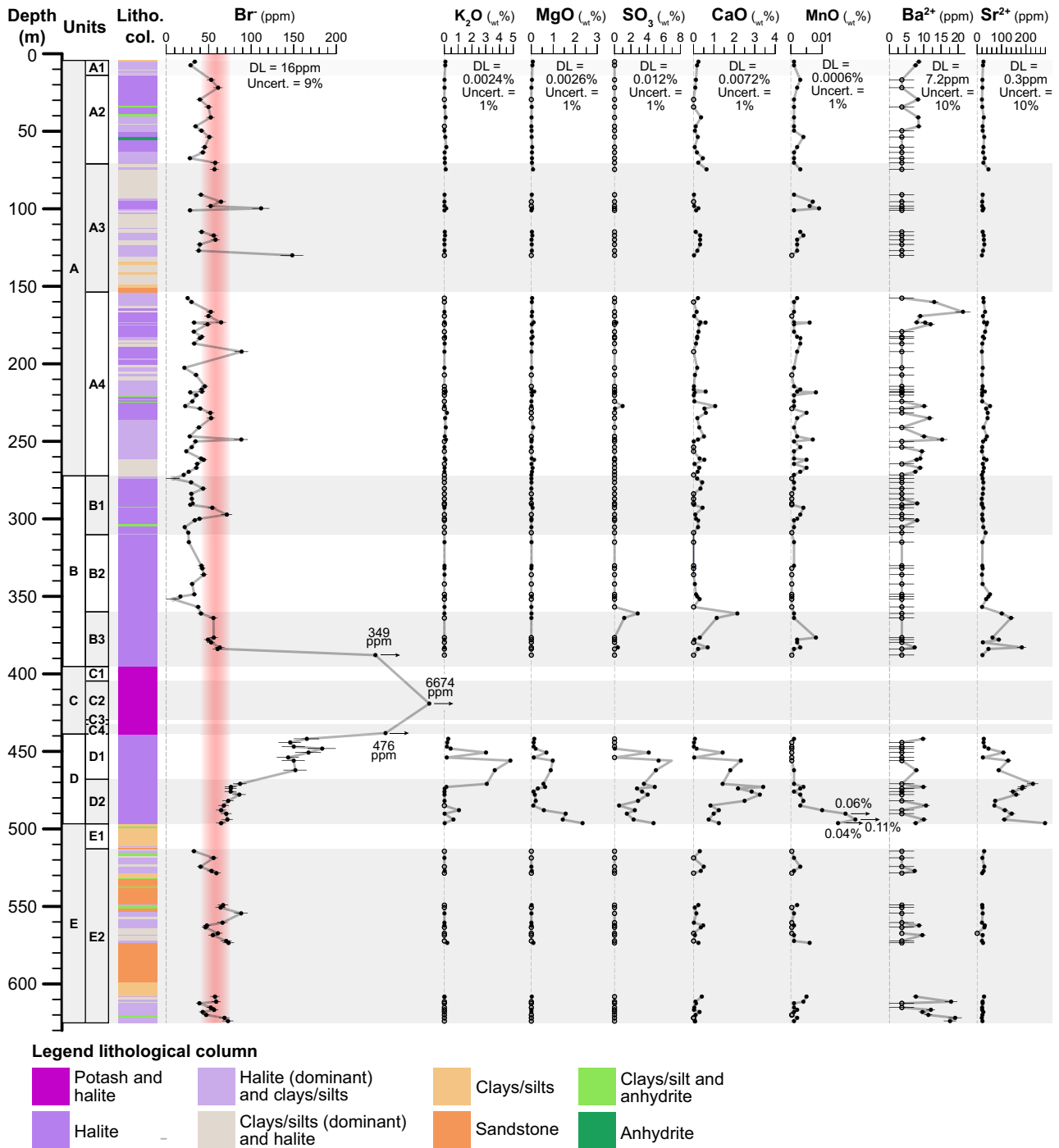


Fig. 8. X-ray fluorescence (XRF) and ion chromatography (IC) analysis of halite of Core A. Br^- , K_2O , MgO , SO_3 , CaO , MnO , Ba^{2+} and Sr^{2+} are presented with detection limits (DL) and relative uncertainty (plotted for minor elements). Unfilled symbols represent measurements below the detection limit plotted at $\text{DL}/2$. The red line for the Br values indicates the commonly accepted range for the limit between meteoric (low) and marine (high) parent fluids (see text for discussion).

Unit ϵ (155 to 125 m) is composed of clastic material with intervals of clay/silt grade clastics and intervals of conglomerates with cobble grade clasts. Some layers of anhydrite are also present.

At 154 m, *Ammonia veneta* and *Bolivina pseudoplicata* are present, along with diatoms.

Unit δ (125 to 67 m) is composed of halite. The facies shows clear, coarse halite at the base,

changing up-section to alternations of fine-grained and coarse-grained halite and to laminated, fine-grained halite at the top of the interval.

Unit γ could not be observed directly by the authors but Rauche & van der Klauw (2011) describe unit γ (67 to 55 m) as mainly consisting of anhydrite with polyhalite and minor amounts of kieserite, carnallite, kainite, tachyhydrite and bischofite, as well as two layers of sylvite, at the top and bottom of the unit. Elemental analyses results performed by Rauche & van der Klauw (2011) (Fig. S2) confirm this interpretation.

Unit β (55 to 37 m) is composed of coarse clear halite.

Core B was not cored above 39 m depth but downhole logging and descriptions by Rauche & van der Klauw (2011) indicate a sharp lithological change at 37 m, marking the lower boundary of unit α (37 to 5.5 m) which is composed of clastic material.

Geochemistry

Core A

Elemental content. The Br content of halite samples (Fig. 8) ranges between 22 and 95 ppm in unit E. These values increase from 69 to 476 ppm in unit D, reach 6674 ppm in unit C, before decreasing to values generally below 70 ppm in units B and A. A few outliers show isolated high values in units B1, A4 and A3. K_2O and MgO values are low except in unit D. SO_3 and CaO of halite samples show low values except in units D and B3. MnO and Ba^{2+} retained in the halite show low values, but the signal is scattered in A4. MnO furthermore shows a peak (up to 1050 ppm) at the base of unit D. Sr^{2+} only shows elevated values in units D and B3.

Based on elemental content measured on the non-evaporitic fraction, the CaO/Al_2O_3 (Fig. 7) ratio reflects the presence of Ca-carbonates and dolomite, as shown by XRD. The MgO/Al_2O_3 ratio correlates with dolomite and magnesite content.

Organic geochemistry. Organic matter analyses (Fig. 9) show that samples from units A, B and E2 mainly belong to type III or a mixture of type II and type III kerogen, with particularly high O index values. Samples of unit E1 evidence a higher H index, representing mainly type I (sapropelic) kerogen.

Modern salt plain

Samples of Recent evaporites taken from the salt plain have a low Br content (46 to 64 ppm) for samples AF19-AF1 and AF19-AS1/2, compatible

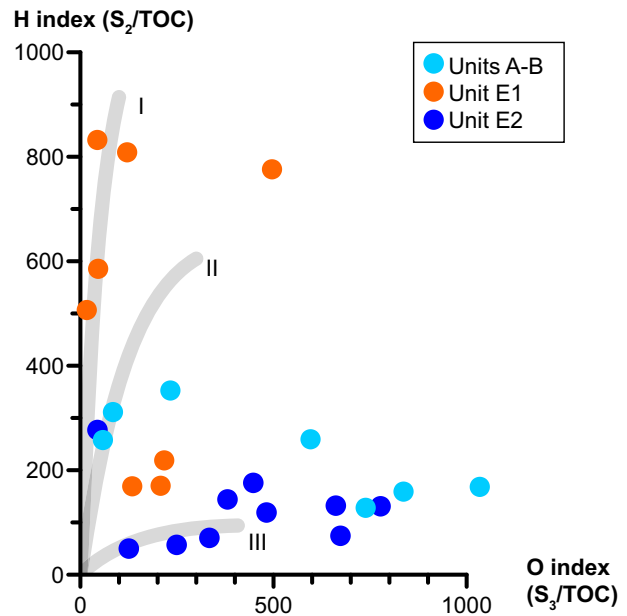


Fig. 9. Van Krevelen diagram of non-evaporitic samples of Core A. It shows the ratio between the H index (S_2/TOC) and O index (S_3/TOC). Grey lines indicate the different types of kerogen. Most samples show low H index (type II and type III kerogen), except in subunit E1 with mainly type I kerogen.

with crystallization from saline continental waters of Lakes Karum and Afdera (position in Fig. 1A and C). Conversely, samples AF19-BS2 and AF19-BS3 taken near small ponds (including one with a red colour, Fig. 4J) indicate elevated Br values of 119 and 208 ppm. These samples also show elevated values of MgO (up to 0.8%) and K_2O (up to 3%), but normal values of Ba^{2+} and Sr^{2+} compared with other samples. These values are compatible with the XRD identification of a small amount of sylvite in AF19-BS3.

Dating

The results of radiocarbon dating from Core A are presented on Figs 3 and S3 and Table S1. Four samples between 10 m and 71 m depth resulted in ages between 1.4 ± 0.2 kyr cal BP and 13.8 ± 0.3 kyr cal BP. A fifth dating at 135 m depth resulted in an age of 35 ± 5 kyr cal BP which is approaching the limit of radiocarbon dating but can still be considered reliable (Hajdas *et al.*, 2021). Two benthic foraminifera samples at 106.2 m and 121.9 m were too small to be dated. Two benthic foraminifera samples at 620.5 m and 620.7 m were too old for radiocarbon dating.

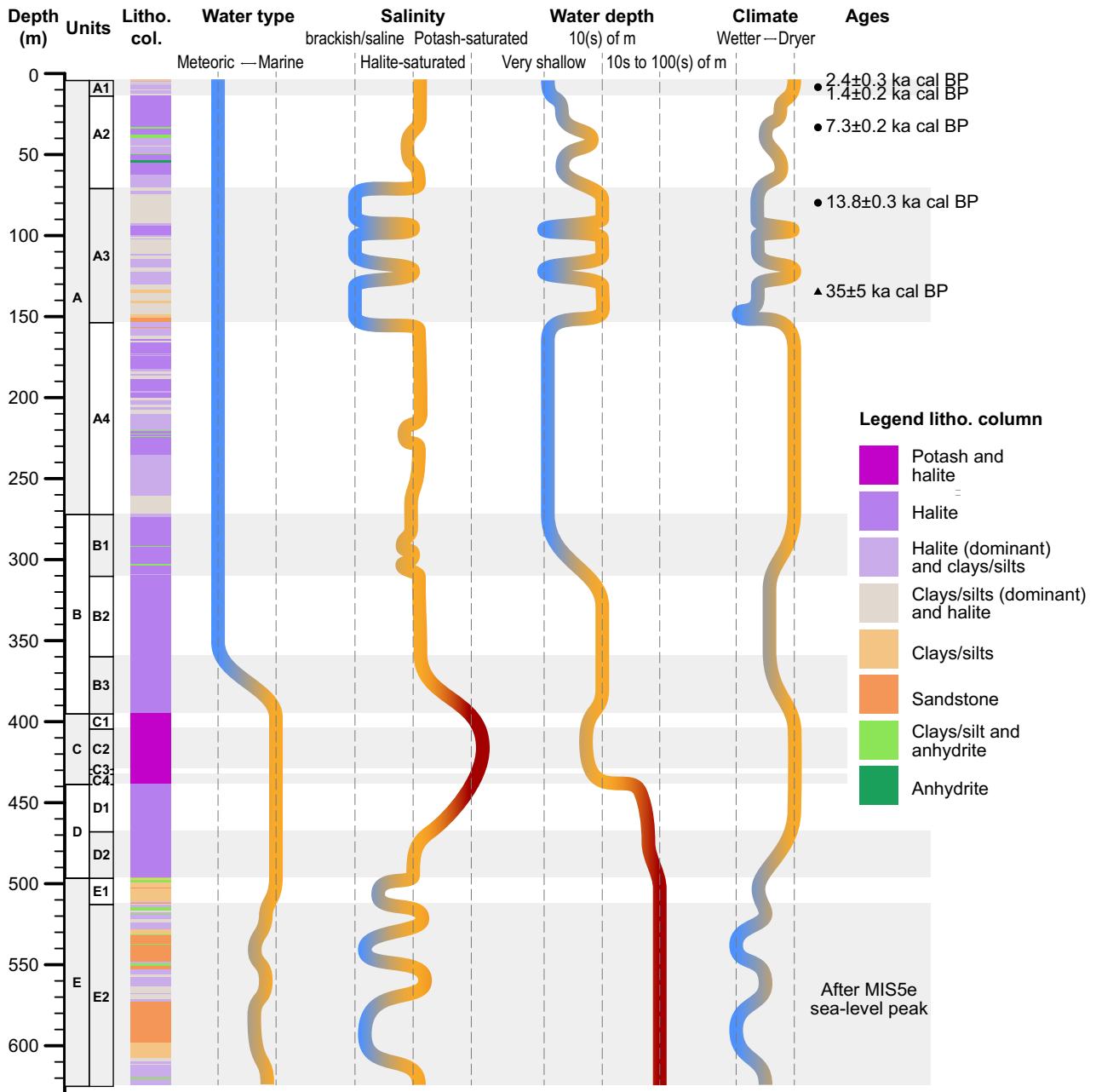


Fig. 10. Palaeoenvironmental (salinity, water depth and meteoric/marine waters) and palaeoclimatic (wet/dry) interpretation of Core A.

DISCUSSION

Chronostratigraphy

Although radiocarbon dating was performed on small samples that might have been transported, the results are coherent and show that subunits A3

to A1 are Late Pleistocene to Holocene in age (Table S1; Fig. 3), representing MIS 3 to MIS 1. The small age reversal at 10 m can be explained by the fact that wood is probably transported to the basin from the margin. The five radiocarbon datings indicate an average sedimentation rate of approximately 4 mm/year in the upper part of unit A.

Palaeo-environmental and palaeo-hydrological interpretation

Restricted marine phase

This phase corresponds to unit E. The Br content of halite alone does not allow to unambiguously distinguish between marine and continental waters as the parent fluid for halite precipitation. However, the values are overall situated within the 45 to 75 ppm range and would be high for a purely continental brine body. The brine is therefore interpreted as a marine water body mixed with high meteoric water input.

Relatively abundant benthic foraminifera (dominated by *Ammonia veneta*), ostracods (*Cyprideis*) and other skeletal fragments were found in subunit E2 (Fig. 3D). They dominantly represent euryhaline species. For example, the species *Cyprideis torosa*, is a coastal and lagoonal euryhaline species, typical of brackish conditions, and occurring frequently in inland saline lakes (e.g. Wouters, 2002). The *pertorosa* subsp. has only been described in lacustrine deposits of supposedly variable salinities of the Danakil Depression (Gramann, 1971). Since the specimens from Core A did not show any signs of carapace nodding that are inferred to be indicative of low salinities (e.g. van Harten, 2000), layers containing *Cyprideis* were probably close to normal marine. This microfaunal interpretation is coherent with the interpretation of the bromine content discussed above, and thus subunit E2 is interpreted to represent a mixed marine–meteoric water body with varying salinity.

The thick clastic intervals, including coarser (sand-grade) beds (Fig. 5N, subunit E2) are interpreted as delta systems. This implies important fluvial input indicating a very wet/humid climate, consistent with the interpretation of a mixed water body. This climate was only interrupted by short drier periods causing an increase in salinity as testified to by the presence of halite and anhydrite layers (Fig. 10).

An alternative interpretation for the presence of coarser-grained intervals in subunit E2 may be that it represents alluvial fans deposited in a continental environment. However, this interpretation is difficult to reconcile with the relatively abundant microfauna that would not be expected in a subaerial fan.

In subunit E1 and a small layer at the base of D2, the presence of dolomite, magnesite, sapropelic organic matter and the absence of fauna and gypsum suggest that this marine-influenced

restricted basin developed into a stratified water body with anoxic conditions in the hypolimnion (Busson & Perthuisot, 1977; Vasconcelos & Mckenzie, 1997; Manzi *et al.*, 2007, 2011, 2018; de Lange & Krijgsman, 2010; Lugli *et al.*, 2010; Dela Pierre *et al.*, 2011, 2012; Roveri *et al.*, 2014; García-Veigas *et al.*, 2018; Tzevahirtzian *et al.*, 2022).

Evaporation phase

This phase corresponds to unit D. The high (>50 ppm) Br content in halite and the high Sr content of unit D unambiguously indicate the dominant presence of marine fluids (Fig. 10). The upward increasing trend in Br content evidences a single cycle of salinity increase throughout the unit, supported by macrofacies and microfacies (see below). The absence of clastic material and the high and increasing salinity indicate arid climatic conditions.

The presence of coarse clear halite crystals (Fig. 6P), such as found in subunit D2, is generally believed to represent bottom-growth halite precipitating from moderately supersaturated fluids (Dellwig, 1955; Li *et al.*, 1996; Kiro *et al.*, 2016; Warren, 2016; Sirota *et al.*, 2017). The inclusion-free halite textures are interpreted in the literature to represent relatively stable chemical conditions, most likely reached under more than a few decimetres of water or to represent syndepositional/early diagenesis recrystallization, late burial diagenesis recrystallization or recrystallization related to deformation (Shearman, 1970; Lowenstein & Hardie, 1985; Schléder & Urai, 2005; Salvany *et al.*, 2007; Lugli *et al.*, 2015). Samples from unit D show no signs of recrystallization, such as curved crystal boundaries forming triple junctions (Lowenstein & Hardie, 1985), and thus are interpreted as primary. Irregular grain boundaries could indicate short-term subaquatic dissolution events.

The lower part of subunit D1, characterized by the alternation of fine-grained and coarse-grained halite, is inferred to reflect similar conditions to the deep hypolimnetic lake floor of the present-day Dead Sea with high halite supersaturation in winter (deposition of halite cumulates) and stratified water with moderate supersaturation during summer (precipitation of bottom-growth halite; Sirota *et al.*, 2017). The fine-grained, laminated halite in the upper part of D1 is inferred to have formed at the air–water interface or just below the thermocline as small cubes or hopper crystals (see Fig. 4D) in highly supersaturated fluids before settling at the basin floor (Lowenstein &

Hardie, 1985; Schreiber & El Tabakh, 2000; Arnon *et al.*, 2016; Kiro *et al.*, 2016; Sirota *et al.*, 2017). The XRD data indicate the presence of polyhalite (coherent with the high K₂O, Ca₂, MgO and SO₄ concentrations shown by XRF, Fig. 8). Polyhalite has been described either as an early diagenetic replacement of anhydrite in marine environments or as a primary mineral (Holser, 1966; Perthuisot, 1971). Polyhalite probably forms the white layers visible in Fig. 6G, on top of fine-grained halite intervals, and may represent a higher supersaturation, thus favouring the hypothesis of primary precipitation. It is unknown whether the kieserite found in the unit is primary or was precipitated within open pore space during the deposition of unit C.

Hyperconcentration phase

This phase corresponds to unit C. The succession of unit C is comparable to the typical potash interval described in the literature and industry reports (see *Geological setting* above), except that the sylvite-rich interval is situated at the base of the unit and not at the top. Holwerda & Hutchinson (1968) and Warren (2016) showed that this sylvite layer is probably secondary, formed by the leaching of carnallite.

Overall, unit C is interpreted to represent an episode during which highly supersaturated brines were present in the Danakil Basin during very arid climatic conditions. Bischofite crystallizes from high salinity brines, with an evaporative concentration factor well above 200 (Harvie *et al.*, 1980; Hardie, 1990). The mineral assemblage (rich in MgSO₄, poor in Ca, devoid of typical meteoric minerals like mirabilite, thenardite, trona and pirsomite) and the high bromine content indicate a marine parent brine and exclude a continental or deep hydrothermal origin for the brines (Hardie, 1984, 1990, 1991; Spencer, 2000).

Saline lake phase

This phase corresponds to unit B. The transition between unit C and unit B is sharp but shows no discontinuity or clastic interval, indicating that the basin was never completely desiccated. The rapidly decreasing bromine content (from 349 to 40 ppm, Fig. 8) up-section in subunit B3 implies a fast freshening-upward trend, indicating a transition to wetter conditions between units C and B. The presence of relatively high bromine values, anhydrite and Sr at the base of subunit B3 suggests a continued marine influence possibly resulting from the leftover brines from the hyperconcentration phase being diluted

by meteoric waters or from residual subsurface flow of Red Sea water.

The coarse clear halite of subunits B3 and B2 indicates direct precipitation on the basin floor. Thin sections (Fig. 6D, E and M) show dissolution surfaces but lack cavities, probably indicating short-lived subaqueous dissolution events. The absence of mosaic textures or fluid and solid inclusions purged to grain boundaries, as well as the presence of synchronous growth structures, indicate that the halite is primary (Hardie *et al.*, 1985; Lowenstein & Hardie, 1985; Schreiber & El Tabakh, 2000). Bromine content in subunit B2 is consistently low and other elements show exceptionally consistent concentrations (Fig. 8), interpreted to represent a perennial and relatively deep meteoric lake under stable chemical conditions, only interrupted by frequent subaqueous dissolution events.

The change of facies to a cloudy texture of chevron halite present in subunit B1 is caused by the presence of fluid inclusions and is believed to indicate short-term variations in temperature, salinity, saturation and growth rate, most likely within a very shallow (a few decimetres) brine pan (Li *et al.*, 1996; Schubel & Lowenstein, 1997; Schreiber & El Tabakh, 2000; Salvany *et al.*, 2007; Kiro *et al.*, 2016; Warren, 2016). This change of microfacies and the appearance of minor clastic intervals, as well as dolomite and magnesite layers, suggest a shallowing-upward trend compared to subunit B2 (Fig. 10).

Saline pan phase

This phase corresponds to subunit A4. The abundance of clastic intervals and of cloudy halite textures, the low Br content and the similarities with facies observed in Recent subunit A1 suggest that subunit A4 was deposited in an episodically inundated continental salt pan, showing very shallow ephemeral water bodies, similar to the present-day environment. This indicates a shallow environment and arid climatic conditions. Varying concentrations of CaO, MnO and Ba²⁺ indicate fluctuating brine chemistry in ephemeral shallow water bodies.

Three samples show higher bromine content. These samples are outliers and do not reflect the general trend, suggesting a short-term and spatially restricted process. Similarly, a very high bromine content is measured in some of the Recent evaporites of the salt plain, sampled near isolated ponds (AF19-BS2 and AF19-BS3 in Fig. 1C – see also Fig. 4J and Table S1). Those ponds show that spatially and, probably,

temporally confined halite precipitation can lead to locally very high Br content values in the Danakil Depression. Three interpretations could explain these high values. Firstly, the subsurface seepage of marine waters through the Amphila gateway or even through fractures of the Buia graben (Fig. 1A) could result in the precipitation of Br-rich halite. Secondly, while the meteoric recycling of marine halite (containing *ca* 60 to 200 ppm of Br) produces halite low in Br content, the leaching of potash minerals with very high (>1000 ppm) Br content can lead to the formation of Br-rich halite, especially if the volume of water is small (Ayora *et al.*, 1994; Taberner *et al.*, 2000). Finally, a hydrothermal origin of the water may explain the presence of Br-rich halite. Vengosh *et al.* (2002) and Nahnybida *et al.* (2009) demonstrated that non-marine (magmatic) hydrothermal water (today produced in the vicinity of the Dallol volcano: Cavalazzi *et al.*, 2019; Kotopoulou *et al.*, 2019; López-García *et al.*, 2020; Otálora *et al.*, 2022) can have a higher Br content than normal meteoric water. Based on the data and observations, all three interpretations are plausible, and it is probably the combination of processes in different parts of the basin that trigger the local and confined precipitation of continental Br-rich halite.

Late lacustrine phase

This phase corresponds to subunits A2 and A3. The clastic-dominated clay-rich subunit A3 indicates an environmental setting influenced by less saturated water. The dominant species composing the foraminiferal assemblage from subunit A3, including *Ammonia* spp., *E. williamsoni*, *E. advenum*, *Q. semiluna* and *H. depressula*, are commonly found in coastal intertidal environments and brackish estuaries (Horton *et al.*, 1999; Debenay & Guillou, 2002; Debenay *et al.*, 2006; Abu-Zied & Hariri, 2016; Mojtahid *et al.*, 2016), hinting at a relatively shallow lake of brackish to saline conditions.

The presence of foraminifera in this interval may indicate transport of propagules or adult individuals by birds from the Red Sea. Even during the MIS 2 lowstand, the Red Sea was situated less than 200 km away. Avian transport of benthic foraminifera over long distances (up to several thousands of kilometres) has been abundantly documented, noticeably for the same shallow-water genera found within unit A2 (*Ammonia* spp., *Quinqueloculina* spp., *Rosalina* spp. and *Bolivina* spp.) (Almogi-Labin *et al.*, 1992;

Patterson *et al.*, 1997; Boudreau *et al.*, 2001; Abu-Zied *et al.*, 2007; Wennrich *et al.*, 2007; Giordana *et al.*, 2011; Riedel *et al.*, 2011; Pint *et al.*, 2017). The absence of foraminiferal test anomalies, which have been linked to the formation of tests under hypersaline conditions (Pint *et al.*, 2017), and the relatively high diversity, point towards a favourable environment, with a brackish to normal marine salinity. The presence of *Guembelitra* sp. (extinct since Cenozoic times) suggests a clastic origin from the Mesozoic sediments abundantly cropping out on the margins of the basin (Rime *et al.*, 2022). Subunit A3 is thus interpreted to have deposited within a brackish lacustrine environment, indicating relatively wet climatic conditions (Fig. 10).

Three intervals of halite are interpreted to represent short episodes with an increase in salinity, probably linked to more arid climatic conditions and a decrease in water depth, as suggested by the cloudy halite facies. The bromine content of these halite layers indicates precipitation in meteoric waters. The two outliers with higher values are interpreted to represent a similar process as the outliers of subunit A4 discussed above.

The halite-rich subunit A2 indicates a more persistent brine pool covering the deepest part of the depression. The lack of clastic material in the two halite intervals dominated by cloudy textures suggests the presence of shallow hypersaline lakes. The more clastic interval between the two halite layers may represent a wetter/fresher period with increased siliciclastic input (Fig. 10).

Modern saline phase

This phase corresponds to subunit A1. The alternating succession of clastic intervals and halite layers with chevron textures in subunit A1 mimics modern deposition in the Danakil Depression (Fig. 4) and represents similar environmental conditions, being a classic saline pan environment under hot and arid conditions (Fig. 10).

From marine to continental settings: a proximal-distal transect

Overall, Core A shows a gradual change from marine-influenced to continental environments (Fig. 10). The lower units (E, D and C) represent the evaporation of marine or mixed marine-meteoric water and, thus, imply a restricted connection with the Red Sea. These three units show a trend of increasing salinity up-section,

from restricted conditions with episodic deposition of halite in unit E to extreme hyperconcentration and deposition of potash in unit C. This trend reflects a single cycle of increasing isolation of the basin. Subunit B3 marks the transition to continental settings with the complete isolation of the basin from the Red Sea. All evaporites of units B2, B1 and A were precipitated from meteoric brines. Facies variations in these upper units reflect changes in climatic conditions rather than changes in basin connectivity. The isolation of the basin was likely driven by the interaction between global sea-level fall and/or tectonic processes between the Danakil Basin and the Red Sea.

These large-scale trends allow correlating the evaporites and associated facies described in Core A with Core B and with the marine Zariga Formation deposited at the basin margin (Fig. 3). The youngest marine sediments cropping out in the Danakil Depression are identified as the upper succession (MIS 5e) of the Zariga Formation and represent the most recent flooding phase of the Danakil Depression (Atnafu *et al.*, 2015; Foubert *et al.*, 2018, 2024; Jaramillo-Vogel *et al.*, 2019; Fig. 2A). No younger marine sediments have been mapped and/or observed in the Danakil Depression (Holwerda & Hutchinson, 1968; Brinckmann & Kürsten, 1971; C.N.R. – C.N.R.S. Afar Team, 1973; Atnafu *et al.*, 2015; Foubert *et al.*, 2018, 2024; Jaramillo-Vogel *et al.*, 2019; Rime *et al.*, 2022; Negga, 2024). Because the lower units of the core (subunits E – B3) represent marine-influenced conditions, whereas the upper units of the core (subunits B2 – A1) all represent exclusively continental conditions, the marine-influenced part of Core A is interpreted to have followed the last marine flooding of the depression, i.e. the same flooding event as the upper succession of the Zariga Formation (Fig. 2A).

None of the recovered sediments of Cores A or B represent open marine conditions such as registered at the margins of the Depression by the deposition of corallgal reefs (Atnafu *et al.*, 2015; Foubert *et al.*, 2018). However, the restricted marine conditions of unit E1 might be time-equivalent to the aragonitic crusts and the laminations of clays and gypsum present on the margins of the depression that are interpreted to represent the start of basin isolation after the latest open marine phase (Jaramillo-Vogel *et al.*, 2019; Figs 3 and 11A). Unit E2, representing a stratified water body with anoxic conditions in the hypolimnion, can be correlated with gypsum deposits covering the youngest corallgal reef

succession at the basin margins (Figs 3 and 11B). Similar correlation between marginal gypsum and anoxic shales/magnesite-rich layers topped by massive halite have been shown in the marine evaporite basin of the Sabkha el Melah (Tunisia) (Perthuisot, 1971; Busson & Perthuisot, 1977) and in the Mediterranean (Manzi *et al.*, 2007, 2011, 2018; de Lange & Krijgsman, 2010; Lugli *et al.*, 2010; Dela Pierre *et al.*, 2011, 2012; García-Veigas *et al.*, 2018). Unit E of Core A is also correlated with the coarser-grained unit ϵ of Core B situated in a more marginal position (Fig. 3).

All units of Cores A and B are thus interpreted to have deposited after the open-marine stage dated to *ca* 128 ka (Foubert *et al.*, 2018, 2024; Jaramillo-Vogel *et al.*, 2019) and should thus be younger. This interpretation of a relative age younger than 128 ka is supported by unpublished industrial seismic data (Pudovskis *et al.*, 2012) showing that the lowermost part of Core A can be correlated with marginal outcrops that record this last flooding and subsequent desiccation phase. The authors are aware of the relative nature of this age model, which highlights the need for future studies that might be able to give absolute age constraints, potentially as part of future drilling in the basin (Foubert *et al.*, 2018, 2024).

Unit D of Core A is interpreted to correlate with unit δ of Core B (Figs 3 and 11C). Both units show the same lithology (nearly pure halite), the same thickness and the same facies succession (coarse, clear halite at the base, fine-grained, laminated halite at the top). Unit C of Core A is interpreted to correlate with unit γ of Core B because both units feature potash minerals (Figs 3 and 11D). The lower part of unit B of Core A is interpreted to correlate with unit β of Core B (Figs 3 and 11E). Both units show similar coarse, clear halite. The transition between units α and β in Core B cannot precisely be correlated to Core A. One hypothesis is that it corresponds to the change in facies between subunits B2 and B1 that is interpreted to represent a reduction in brine depth (Figs 3 and 10, see text above). Unit α of Core B is interpreted to correspond to the time-equivalent of units A to possibly B1 of Core A, albeit representing a more proximal depositional environment (Fig. 11F to H).

Mechanism of evaporite formation in the Danakil Depression

Palaeo-environmental and palaeo-hydrological interpretations show that the evaporites in the

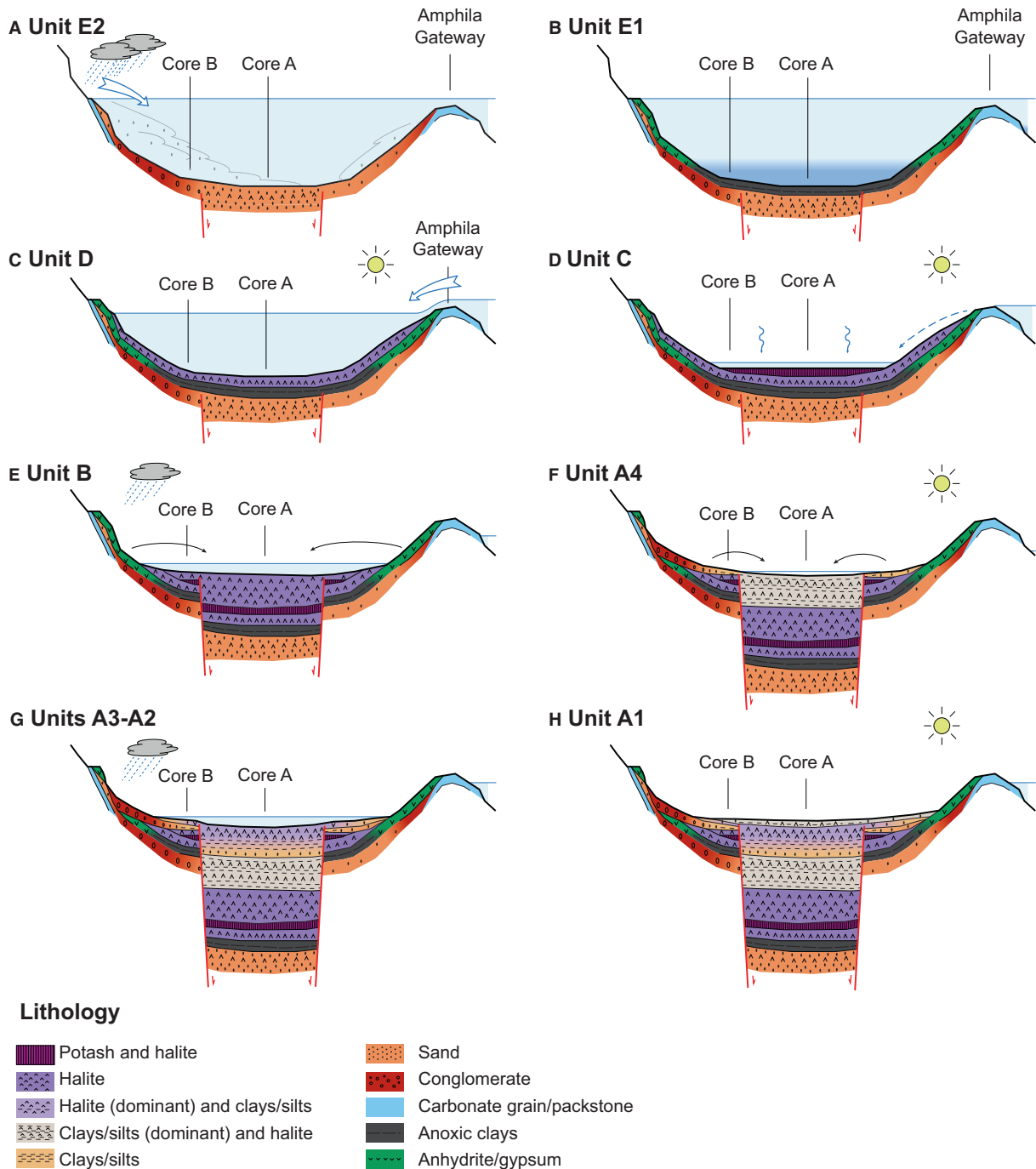


Fig. 11. Depositional model for the Danakil Basin illustrating palaeo-environmental conditions since the deposition of unit E2. The diagrams are not to scale and have strong vertical exaggeration. The tectonic structure is simplified and hypothetical. (A) Restricted marine stage shortly after the Marine Isotope Stage (MIS) 5e highstand. A wet climate results in increased fluvial clastic input into the basin. (B) The basin becomes more restricted and stratified with the deposition of gypsum on the margins and anoxic clays in the central part. (C) Evaporation stage. Halite starts to precipitate under arid conditions. The basin remains flooded under a certain depth of marine brine supplied through the Amphila Gateway. (D) Hyperconcentration stage. The connection with the Red Sea reduces, the brine depth decreases and potash minerals precipitate in the central part of the basin. (E) Saline lake stage. Meteoric water dissolves the evaporites on the margins and recycles them in the central part of the basin. (F) Saline pan stage. Dry climatic conditions induce an environment comparable to the present-day situation. (G) Late lacustrine stage. A wet climate triggers the establishment of a brackish/saline lake that becomes hypersaline in its late phase. (H) Modern saline pan.

upper (units B and A) and lower (units E, D and C) parts of the core were precipitated under two different scenarios.

Evaporites of units E, D and C formed from direct evaporation of seawater. The significant thickness of evaporites with a continuous increasing salinity trend up-section suggests that the connection between the basin and the Red Sea was not closed by one rapid and distinct event (which would have produced only a few metres of halite; Usiglio, 1849) but that the basin was continuously fed by the Red Sea by shallow spill-over. The basin must have reached a point where the influx of seawater from the Red Sea nearly equilibrated: (i) the loss by evaporation; (ii) potential reflux; and (iii) freshening of the brine by meteoric waters and precipitation, allowing a constant influx of ions to the basin and the precipitation of >100 m of evaporites.

Unit E correlates with aragonite crusts and gypsum found on top of the marine deposits at the margin, indicating that the water level was at or near maximum sea level during the first phase of deposition (Figs 10, 11A and 11B). Unit D of Core A and unit δ of Core B show the same lithology, facies and thickness, suggesting the presence of a homogenous brine body with a significant depth (tens to hundreds of metres, Figs 10 and 11C). Conversely, the mineralogy and facies of unit C of Core A and unit γ of Core B differ. The thickness of the latter is also significantly smaller. This suggests a lowering of the brine level during the deposition of unit C, indicating that evaporation was potentially, at least temporarily, more important than inflow. The brine body was nevertheless covering a relatively large extent because this potash unit has been traced across vast areas of the basin by core and seismic data provided by commercial companies (Holwerda & Hutchinson, 1968; Rauche & van der Klauw, 2011; Pudovskis *et al.*, 2012; Warren, 2016). This suggests that the depth of the brine was not extremely shallow but could reach at least a few metres (Figs 10 and 11D). Units E, D and C thus show a large-scale shallowing-upward trend, along with the trend of increasing salinity up-section, but these evaporites all represent direct precipitation from marine-influenced brines and the source of ions is therefore primarily marine.

Conversely, unit B was mainly formed by meteoric water influx in a perennial lake. Unit β of Core B and the lower part of unit B of Core A show the same lithology and facies. This

supports the interpretation of a relatively deep and extensive water body during the initial phase of deposition of the unit, with a water depth possibly reaching several tens of metres (Figs 10 and 11E), such as suggested by facies analyses and geochemical data (see above). The presence of this relatively large meteoric lake also indicates wetter conditions than during the deposition of units A4 and C. Because meteoric water does not have enough salinity to precipitate halite (Kebede *et al.*, 2008; Meaza *et al.*, 2019), the high salinity resulting in halite precipitation in the central part of the basin must have been caused by the dissolution of older evaporites at the margin of the basin (Fig. 11E), as observed today. This assumption is supported by the much smaller thickness of unit β in Core B, situated in a more marginal setting, and by the description of vertical dissolution cavities in a more marginal core (DK-11-11, see Fig. 1C for position; Warren, 2016) which suggests that the upper part of the unit β in Core B was dissolved by fresher waters. The lower thickness of unit β in Core B compared to unit B in Core A can also indicate that: (i) this part of the basin was flooded for a shorter amount of time; (ii) this part of the basin was flooded but situated above the epilimnion and *halite focusing* (e.g. Sirota *et al.*, 2018; Kirkham *et al.*, 2020) concentrated the deposition in the central part of the basin; and (iii) available accommodation was smaller. Whatever the reason for reduced halite precipitation at the margin of the basin, it should be highlighted that halite deposition was concentrated in the central part of the basin (Fig. 11E). These waters might also have partly recycled older evaporites deposited on the margins during previous flooding events and uplifted by tectonic movements or transported by shallow hydrothermal circulation. Evaporite recycling by meteoric waters has also been described in the Lorca Basin in Spain (Taberner *et al.*, 2000). The greater thickness of units B and A in Core A compared with the equivalent deposits of Core B (44 m versus 12 m) stress the importance of available accommodation for the deposition of thick evaporite deposits (Fig. 11E to H). As the potash units of Cores A and B deposited at nearly the same elevation in shallow waters and are now found at 395 m and 55 m depth, respectively, a relative subsidence of *ca* 370 m occurred since the deposition of the potash. This value is comparable with the estimations of Bastow *et al.* (2018) and Hurman *et al.* (2023).

Relevance of the Danakil Basin for the understanding of large evaporite deposits

The Danakil evaporites cover a significantly smaller area than classical salt giants. The Pleistocene Danakil Sea covered a surface area of approximately 9000 km², which is more than two orders of magnitude smaller than the Messinian basins of the Mediterranean (Warren, 2010) and the total volume of evaporites is thus much smaller. However, their significant thickness (>600 m described in this study but more evaporites are inferred to be present at greater depth: Holwerda & Hutchinson, 1968; Behle *et al.*, 1975; Makris & Ginzburg, 1987; Pudovskis *et al.*, 2012), their marine origin, their occurrence in an active rift setting and their high halite percentage do mimic some aspects of some ancient salt giants; for example, the Carboniferous to Permian evaporites of the Barents Sea (Hassaan *et al.*, 2020), the Permo-Triassic Zechstein evaporites (Soto *et al.*, 2017), the Triassic to Jurassic evaporites of the northern Atlantic (Holser *et al.*, 1988; Decalf & Heyn, 2023), the Jurassic Louann Salt of the Gulf of Mexico (Hudec *et al.*, 2013), the Aptian salt of the southern Atlantic (Kukla *et al.*, 2018; Rodriguez *et al.*, 2018; Célini *et al.*, 2024; Pichat *et al.*, 2024) or the Miocene Red Sea evaporites (Hughes & Beydoun, 1992; Orszag-Sperber *et al.*, 1998; Smith & Santamarina, 2022). Some of the processes forming these salt giants will thus possibly be similar to those that formed the Danakil evaporites. The Danakil evaporites may therefore be considered as a possible analogue for some ancient salt giants.

The Danakil evaporites being very young (and still forming nowadays) allow a better understanding of some aspects of their formation. The topography, the hydrology, the relative sea level of the neighbouring oceanic basin (Grant *et al.*, 2014), the regional palaeoclimatic conditions (Gillespie *et al.*, 1983; Fleitmann *et al.*, 2011; Rosenberg *et al.*, 2011; Tierney *et al.*, 2017; Lamb *et al.*, 2018; Nicholson *et al.*, 2020; Schaebitz *et al.*, 2021; Foerster *et al.*, 2022), the tectonic structure and movements of the basin (Bastow *et al.*, 2018; Hurman *et al.*, 2023), as well as the general tectonic context (Viltres *et al.*, 2020; Rime *et al.*, 2023) are indeed better known than for older counterparts.

Accumulation rates, certainly in evaporites, are often a topic of debate and may vary significantly, reaching very high rates (Lensky *et al.*, 2005; Manzi *et al.*, 2012; Peel, 2019; Sirota *et al.*, 2021). The present study suggests that 625 m of evaporite-dominated sediments were deposited in

less than 128 kyr in the Danakil Depression, resulting in minimum average accumulation rates of 4.9 mm/year. This accumulation rate is the same order of magnitude as the overall *ca* 2.5 mm/year estimated for the *ca* 1.8 km of halite-dominated Messinian Salinity Crisis deposits in the Levant basin (Meilijson *et al.*, 2019) and the *ca* 5 mm/year of the *ca* 2.5 km of evaporites of the Santos Basin (Davison *et al.*, 2012). It highlights the possibility of depositing several hundreds of metres of evaporites within short (<128 kyr) periods. In the case of Danakil, it corresponds to one single desiccation cycle after marine flooding.

The precise rate of deposition of units D, C and B, composed almost entirely by salts, is not known due to the lack of age constraints. However, cycles between fine-grained and coarse-grained halite or between halite and shale/anhydrite are known to represent annual cycles in the Dead Sea and the evaporites deposited during the Messinian Salinity Crisis (Manzi *et al.*, 2012; Sirota *et al.*, 2017). Cycles are also visible in the marine units D1 and C, representing the most saturated brine recorded in the Danakil evaporites. At the base of subunit D1, cycles between fine-grained and coarse-grained halite can be observed. Most of them are between 1 cm and 6 cm thick (Fig. 5K). Cycles in the uppermost 9 m of D1 (Fig. 5J) can be up to 25 cm thick. Subunits C3, C2 and C1 also present irregular cycles up to 30 cm thick. The annual duration of these cycles cannot be demonstrated but, if they do represent annual or bi-annual cycles, they would be comparable with other records from around the world featuring cyclic evaporite deposits, including the 4.5 to 7.5 cm/year measured in the Dead Sea (Sirota *et al.*, 2021) and the 15 cm/year observed in the Messinian Realmonte salt mine (Manzi *et al.*, 2012). Higher rates reaching 100 cm/year have even been proposed for the Luann Salt of the Gulf of Mexico and the MacLeod Basin of Western Australia (Logan, 1987; Davison *et al.*, 2012; Peel, 2019). A very high deposition rate of evaporites during the final phase of basin isolation and the most saturated brine stage is therefore plausible but should be confirmed by future studies.

Several authors have argued against a solar evaporation model for salt giants (Scribano *et al.*, 2017; Hovland *et al.*, 2018a,b; Debure *et al.*, 2019; Qin *et al.*, 2023), proposing that one single desiccation cycle of 1000 m of water could only produce *ca* 15 m of evaporites and that too many cycles would be necessary to produce kilometre-thick deposits. These models do not

consider a possible protracted supply of seawater during the evaporation stage, as shown by numerous other authors (e.g. Hardie, 1990; Kirkland *et al.*, 2000; Meijer, 2006; Krijgsman & Meijer, 2008; Montaron & Tapponnier, 2010; Topper & Meijer, 2013; Simon & Meijer, 2015, 2017; Montaron, 2016; Konstantinou *et al.*, 2023). The example of the Danakil Depression shows that, under suitable conditions, a single, short cycle of direct evaporation of seawater may produce *ca* 60 m of halite and *ca* 40 m of potash, whilst the following periods of meteoric reworking can add almost 400 m of evaporite-dominated sediments in less than 128 kyr.

Some authors have suggested that salt giants were produced by deep hydrothermal processes, including serpentinization of the mantle (Scribano *et al.*, 2017; Hovland *et al.*, 2018a,b; Debure *et al.*, 2019; Qin *et al.*, 2023). Hovland *et al.* (2018b) and Johnsen *et al.* (2021) used the Danakil evaporites as an example of this process. The facies and mineralogy of these evaporites, as well as the general geological history of the basin, show that no deep hydrothermal processes are needed to explain their deposition. The facies of the evaporites are all compatible with known examples of solar evaporites. Solar evaporation alone can thus satisfactorily explain the upper 625 m of evaporite-dominated sediments of the Danakil Depression. In addition, the mineralogy of unit C (kieserite, kainite and polyhalite) is inconsistent with known hydrothermal examples (Hardie, 1990). Finally, the proven flooding of the depression by the Red Sea and its consecutive isolation (Holwerda & Hutchinson, 1968; Brinckmann & Kürsten, 1971; Atnafu *et al.*, 2015; Foubert *et al.*, 2018; Jaramillo-Vogel *et al.*, 2019; Endeshaw, 2024) provides a robust source for these evaporites. A high bromine content in some isolated halite may indicate that some of the halite was potentially mobilized by deep hydrothermal fluids. However, this geochemical signal does not represent a major contribution to the Danakil evaporites. This is coherent with the results of Talbot (2008) describing only: “minor local additions of hydrothermal salts” on the Dallol dome. Moreover, according to the model of Otálora *et al.* (2022) and the present study, these hydrothermal fluids gained salinity by the dissolution of older, solar precipitated evaporites and reprecipitated by solar evaporation at the surface. Therefore, even if hydrothermal processes did play a role, no deep serpentinization processes are required. Such serpentinization would also

be very difficult to achieve because the Moho in the Danakil Depression is situated at least at 14 km depth (Makris & Ginzburg, 1987; Wang *et al.*, 2021; Ahmed *et al.*, 2022; Gauntlett *et al.*, 2024). At basin-scale, the deep hydrothermal influence is therefore probably minor, being only localized in specific spots within the vicinity of the Dallol volcano or other hot springs.

CONCLUSIONS

Based on the multiproxy analysis of two sediment cores, the Late Pleistocene to Holocene evaporitic sedimentary record of the Danakil Basin could be unravelled and summarized in the following conclusions:

- 1 The uppermost 625 m of basin fill of the Danakil Depression are mainly formed by halite and subordinate clastic sediments. The great thickness of these deposits, their occurrence in an active rift setting and their high halite percentage mimic some aspects of some ancient large evaporite deposits, including some salt giants. Some of the processes that formed, and are still forming, the Danakil evaporites may be comparable with the ones that formed some of these ancient deposits.

- 2 The record can be divided into five different units. The lowermost unit (E) shows clastic and evaporitic sedimentation in a restricted marine basin during wet climatic conditions. Unit D corresponds to the evaporation of seawater in an arid climate precipitating mainly halite. Unit C is characterized by the precipitation of potash minerals in a highly saturated brine of marine origin. The lowermost part of unit B records the youngest marine brines and thus the last connection of the basin with the Red Sea. The rest of unit B depicts the filling of the basin by a meteoric lake recycling older marine evaporites. Unit A represents the deposition of evaporites and clastic sediments in a continental salt pan and a brackish/saline lake.

- 3 Two different main mechanisms of formation of the Danakil evaporites are identified. More than 100 m of evaporites were deposited by the direct evaporation of seawater (units C, D and E) while recycling of marine evaporites from the margins towards the centre of the basin, together with subsidence, played a major role after the isolation of the basin (units A and B).

- 4 The Danakil evaporites show that a significant thickness of evaporite-dominated sediments (>600 m) may accumulate in a very short

amount of time (<128 kyr) following a single marine flooding and desiccation event.

This study highlights the scientific value of the of Danakil evaporites for understanding mechanisms of evaporite formation driven by local, regional and global processes. This study also provides the basis for future regional studies in the Danakil Basin focusing on chronostratigraphy, cyclicity of the evaporites, hydrology and fluid flow patterns, geochemistry, micropaleontology, geomicrobiology, palaeoclimatology, tectonics and opening/closure mechanisms of a restricted basin (Foubert *et al.*, 2018, 2024).

ACKNOWLEDGEMENTS

This study was funded by the Swiss National Science Foundation (SNF projects SERENA – SEdimentary REcord of the Northern Afar 200021_163114 and CONNECT: Paleo-Connectivity and Pale-Hydrological change in an initial rift basin. SNF project 200020_212903). We are grateful to the University of Fribourg (Switzerland), Addis Ababa University (Ethiopia), the Ethiopian Ministry of Mines, the former Ethiopian Ministry of Mines and Energy, the former Geological Survey of Ethiopia, Circum Minerals, former Allana Potash and Yara Dallol for their support. We warmly thank the former Ethiopian Ministry of Mines for sharing with us the data of Core A and for the initiative of collaboration between potash companies and universities, as well as Jason Wilkinson for giving us access to Core B. We sincerely acknowledge Ermias Gebru, Samuel Getachew and Million Alemayehu that helped with the sampling of the core. We warmly thank Alexandre Salzmänn (sample preparation), Jean Rodier (XRF), Patrick Dietsche (thin sections), Bernard Grobety (XRD) and Haghypour Negar (radiocarbon datings) for their help during the preparation and analysis of the samples. Géraldine Zimmerli, Janine Sturny and Xenia Haberditz also worked meticulously on the preparation of the halite samples. We acknowledge Fabio Francescangeli for his advice on foraminifera. We thank Volker Liebetrau for trying to date the foraminifera. We acknowledge the work of two anonymous reviewers and Stephen Lokier (editor) whose comments significantly helped to improve the paper. We thank David Jaramillo-Vogel, Addis Endeshaw, Ermias Gebru, Eva De Boever, Juan-Carlos Braga, Pia Wyler, Xenia Haberditz, Émilie Mailard, Taffesse Birhanu, the Ethioder team, as well

as the regional and local administration of the Afar for their help and support during fieldwork. We furthermore thank Géraldine Zimmerli, Eva De Boever, David Jaramillo-Vogel, Adeline Marro and Valentina Beccari for help, comments and tips. This study was produced in the framework of a PhD thesis and Lisa McNeil, Derek Keir, Jon Mosar and Joël Ruch, who were part of the examination committee of this thesis, are acknowledged for their comments and corrections. Open access funding provided by Université de Fribourg.

DATA AVAILABILITY STATEMENT

The newly produced data that supports the findings of this study are available in the supplementary material of this article. Data from industrial companies and the former Ethiopian Ministry of Mines are not shared because of confidentiality reasons.

REFERENCES

- Abu-Zied, R.H. and Hariri, M.S.B. (2016) Geochemistry and benthic foraminifera of the nearshore sediments from Yanbu to Al-Lith, eastern Red Sea coast, Saudi Arabia. *Arab. J. Geosci.*, **9**, 245.
- Abu-Zied, R.H., Keatings, K.W. and Flower, R.J. (2007) Environmental controls on foraminifera in Lake Qarun, Egypt. *J. Foraminifer. Res.*, **37**, 136–149.
- Ahmed, A., Doubre, C., Leroy, S., Keir, D., Pagli, C., Hammond, J.O.S., Ayele, A., Be de Berc, M., Grunberg, M., Vergne, J., Pestourie, R., Mamo, D., Kibret, B., Cubas, N., Lavayssière, A., Janowski, M., Lengliné, O., La Rosa, A., Chambers, E.L. and Illsley-Kemp, F. (2022) Across and along-strike crustal structure variations of the western Afar margin and adjacent plateau: insights from receiver functions analysis. *J. Afr. Earth Sci.*, **192**, 570.
- Almogi-Labin, A., Perelis-Grossovicz, L. and Raab, M. (1992) Living Ammonia from a hypersaline inland pool, Dead Sea area, Israel. *J. Foraminifer. Res.*, **22**, 257–266.
- Arnon, A., Selker, J.S. and Lensky, N.G. (2016) Thermohaline stratification and double diffusion diapycnal fluxes in the hypersaline Dead Sea. *Limnol. Oceanogr.*, **61**, 1214–1231.
- Atnafu, B., Kidane, T., Foubert, A., Jaramillo-Vogel, D., Schaegis, J.C. and Henriët, J.P. (2015) Reading history from Afar. *Eos*, **98**, 12–15.
- Ayora, C., Garcia-Veigas, J. and Pueyo, J.J. (1994) The chemical and hydrological evolution of an ancient potash-forming evaporite basin as constrained by mineral sequence, fluid inclusion composition, and numerical simulation. *Geochim. Cosmochim. Acta*, **58**, 3379–3394.
- Babel, M. and Schreiber, B.C. (2014) Geochemistry of evaporites and evolution of seawater. In: *Treatise on Geochemistry* (Eds Holland, H.D. and Turekian, K.), 2nd edn, pp. 483–560. Elsevier, Oxford.

- Barberi, F. and Varet, J.** (1970) The Erta Ale volcanic range (Danakil depression, northern afar, Ethiopia). *Bull. Volcanol.*, **34**, 848–917.
- Barberi, F., Borsi, S., Ferrara, G., Marinelli, G. and Varet, J.** (1970) Relations between tectonics and magmatology in the northern Danakil Depression (Ethiopia). *Philos. Trans. R. Soc. Lond.*, **267**, 293–311.
- Barberi, F., Borsi, S., Ferrara, G., Marinelli, G., Santacroce, R., Tazieff, H. and Varet, J.** (1972) Evolution of the danakil depression (Afar, Ethiopia) in light of radiometric age determinations. *J. Geol.*, **80**, 720–729.
- Bastow, I.D. and Keir, D.** (2011) The protracted development of the continent-ocean transition in Afar. *Nat. Geosci.*, **4**, 248–250.
- Bastow, I.D., Booth, A.D., Corti, G., Keir, D., Magee, C., Jackson, C.A.-L., Warren, J., Wilkinson, J. and Lascialfari, M.** (2018) The development of late-stage continental breakup: seismic reflection and borehole evidence from the Danakil Depression, Ethiopia. *Tectonics*, **37**, 2848–2862.
- Beccaluva, L., Bianchini, G., Natali, C. and Siena, F.** (2009) Continental flood basalts and mantle plumes: a case study of the Northern Ethiopian Plateau. *J. Petrol.*, **50**, 1377–1403.
- Behle, A., Makris, J., Baier, B. and Delibasis, N.** (1975) Salt thickness near Dallol (Ethiopia) from seismic reflection measurements and gravity data. In: *Afar Depression of Ethiopia: Proceedings of an International Symposium on the Afar Region and Related Rift Problems* (Eds Pilger, A. and Rösler, A.), pp. 156–167. *E. Schweizerbart'sche Verlagsbuchhandlung*, Stuttgart.
- Bekele, A. and Schmerold, R.** (2020) Characterization of brines and evaporite deposits for their lithium contents in the northern part of the Danakil Depression and in some selected areas of the Main Ethiopian Rift lakes. *J. Afr. Earth Sci.*, **170**, 103904.
- Belilla, J., Moreira, D., Jardillier, L., Reboul, G., Benzerara, K., López-García, J.M., Bertolino, P., López-Archilla, A.I. and López-García, P.** (2019) Hyperdiverse archaea near life limits at the polyextreme geothermal Dallol area. *Nat. Ecol. Evol.*, **3**, 1552–1561.
- Beyth, M.** (1972) Paleozoic-mesozoic sedimentary basin of mekele outlier, Northern Ethiopia. *Am. Assoc. Pet. Geol. Bull.*, **56**, 2426–2439.
- Beyth, M.** (1973) Interpretation of the stratigraphy of northern Ethiopia according to the model of plate tectonics. *Geology*, **1**, 81–82.
- Beyth, M.** (1978) A comparative study of the sedimentary fills of the Danakil depression (Ethiopia) and Dead Sea rift (Israel). *Tectonophysics*, **46**, 357–367.
- Blamey, N.J.F. and Brand, U.** (2019) Atmospheric gas in modern and ancient halite fluid inclusions: a screening protocol. *Gondwana Res.*, **69**, 163–176.
- Boeke, H.E.** (1908) Über das Krystallisationsschema der Chloride, Bromide, Jodide von Natrium, Kalium und Magnesium, sowie über das Vorkommen des Broms und das Fehlen von Jod in den Kalisalzlagernstätten. *Z. Kristallogr. Cryst. Mater.*, **45**, 346–391.
- Bonatti, E., Emiliani, C., Ostlund, G. and Rydell, H.** (1971) Final desiccation of the Afar Rift, Ethiopia. *Science*, **172**, 468–469.
- Boudreau, R.E.A., Patterson, R.T., Dalby, A.P. and McKillop, W.B.** (2001) Non-marine occurrence of the foraminifer *Criboelphidium gunteri* in northern Lake Winnipegosis, Manitoba, Canada. *J. Foraminifer. Res.*, **31**, 108–119.
- Braitsch, O. and Herrmann, A.G.** (1963) Zur Geochemie des Broms in salinaren Sedimenten. *Geochim. Cosmochim. Acta*, **27**, 361–391.
- Brennan, S.T., Lowenstein, T.K. and Cendon, D.I.** (2013) The major-ion composition of Cenozoic seawater: the past 36 million years from fluid inclusions in marine halite. *Am. J. Sci.*, **313**, 713–775.
- Brinckmann, J. and Kürsten, M.** (1971) Stratigraphie und Tektonik der Danakil-Senke (NE-Ätiopien). *Beihefte zum Geologischen Jahrbuch*, **116**, 5–87.
- Brookins, D.G., Register, J.K. and Krueger, H.W.** (1980) Potassium-argon dating of polyhalite in southeastern New Mexico. *Geochim. Cosmochim. Acta*, **44**, 635–637.
- Busson, G. and Perthuisot, J.P.** (1977) Interet de la Sebkh el Melah (sud-Tunisien) pour l'interpretation des series evaporitiques anciennes. *Sed. Geol.*, **19**, 139–164.
- C.N.R. - C.N.R.S. Afar Team** (1973) Geology of Northern Afar (Ethiopia). *Rev. Géogr. Phys. Géol. Dynam.*, **14**, 443–490.
- Cavalazzi, B., Barbieri, R., Gómez, F., Capaccioni, B., Olsson-Francis, K., Pondrelli, M., Rossi, A.P., Hickman-Lewis, K., Agangi, A., Gasparotto, G., Glamoclija, M., Ori, G.G., Rodriguez, N. and Hagos, M.** (2019) The Dallol Geothermal Area, Northern Afar (Ethiopia)—an exceptional planetary field analog on earth. *Astrobiology*, **19**, 553–578.
- Célini, N., Pichat, A. and Ringenbach, J.-C.** (2024) Salt tectonics synchronous with salt deposition in the Santos Basin (Ariari Formation, Brazil). *Earth Planet. Sci. Lett.*, **641**, 118853.
- Cendón, D.I., Peryt, T.M., Ayora, C., Pueyo, J.J. and Taberner, C.** (2004) The importance of recycling processes in the Middle Miocene Badenian evaporite basin (Carpathian foredeep): palaeoenvironmental implications. *Palaeogeogr. Palaeoclimatol. Palaeoecol.*, **212**, 141–158.
- Cerveny, R.S., Lawrimore, J., Edwards, R. and Landsea, C.** (2007) Extreme weather records: compilation, adjudication, and publication. *Bull. Am. Meteorol. Soc.*, **88**, 853–860.
- Coulié, E., Quidelleur, X., Gillot, P.-Y., Courtillot, V., Lefevre, J.-C. and Chiesa, S.** (2003) Comparative K–Ar and Ar/Ar dating of Ethiopian and Yemenite Oligocene volcanism: implications for timing and duration of the Ethiopian traps. *Earth Planet. Sci. Lett.*, **206**, 477–492.
- Davison, I., Anderson, L. and Nuttall, P.** (2012) Salt deposition, loading and gravity drainage in the Campos and Santos salt basins. *Geol. Soc. London Spec. Publ.*, **363**, 159–174.
- Debenay, J.-P. and Guillou, J.-J.** (2002) Ecological transitions indicated by foraminiferal assemblages in paralic environments. *Estuar. Res. Federation Estuaries*, **25**, 1107–1120.
- Debenay, J.P., Bicchi, E., Goubert, E. and Arminot Du Châtelet, E.** (2006) Spatio-temporal distribution of benthic foraminifera in relation to estuarine dynamics (Vie estuary, Vendée, W France). *Estuar. Coast. Shelf Sci.*, **67**, 181–197.
- Debure, M., Lassin, A., Marty, N.C., Claret, F., Virgone, A., Calassou, S. and Gaucher, E.C.** (2019) Thermodynamic evidence of giant salt deposit formation by serpentinization: an alternative mechanism to solar evaporation. *Sci. Rep.*, **9**, 720.
- Decalf, C.C. and Heyn, T.** (2023) Salt geometry in the Central Basin of the Nova Scotia passive margin, offshore Canada based on new seismic data. *Mar. Pet. Geol.*, **149**, 106065.

- Dela Pierre, F., Bernardi, E., Cavagna, S., Clari, P., Gennari, R., Irace, A., Lozar, F., Lugli, S., Manzi, V., Natalicchio, M., Roveri, M. and Violanti, D.** (2011) The record of the Messinian salinity crisis in the Tertiary Piedmont Basin (NW Italy): The Alba section revisited. *Palaeogeogr. Palaeoclimatol. Palaeoecol.*, **310**, 238–255.
- Dela Pierre, F., Clari, P., Bernardi, E., Natalicchio, M., Costa, E., Cavagna, S., Lozar, F., Lugli, S., Manzi, V., Roveri, M. and Violanti, D.** (2012) Messinian carbonate-rich beds of the Tertiary Piedmont Basin (NW Italy): microbially-mediated products straddling the onset of the salinity crisis. *Palaeogeogr. Palaeoclimatol. Palaeoecol.*, **344–345**, 78–93.
- Dellwig, L.F.** (1955) Origin of the Salina Salt of Michigan. *J. Sed. Res.*, **25**, 83–110.
- Eagles, G., Gloaguen, R. and Ebinger, C.** (2002) Kinematics of the Danakil microplate. *Earth Planet. Sci. Lett.*, **203**, 607–620.
- Earth Resources Observation and Science (EROS) Center.** (2018) Shuttle Radar Topography Mission (SRTM) 1 Arc-Second Global.
- Endeshaw, A.** (2024) Pleistocene corals of the Danakil depression: taxonomy and palaeoecology (North Afar, Ethiopia). PhD Thesis, University of Fribourg.
- Ercan, H.Ü., Karakaya, M.C., Bozdog, A., Karakaya, N. and Delikan, A.** (2019) Origin and evolution of halite based on stable isotopes ($\delta^{37}\text{Cl}$, $\delta^{81}\text{Br}$, $\delta^{11}\text{B}$ and $\delta^7\text{Li}$) and trace elements in Tuz Gölü Basin, Turkey. *Appl. Geochem.*, **105**, 17–30.
- Faure, H. and Roubet, C.** (1968) Découverte d'un biface acheuléen dans les calcaires marins du golfe pléistocène de l'Afar (Mer Rouge, Ethiopie). *Comptes Rendus Hebdomadaires séances l'Acad. Sci. Série D*, **267**, 18–21.
- Fazzini, M., Bisci, C. and Billi, P.** (2015) The climate of Ethiopia. In: *Landscapes and Landforms of Ethiopia* (Ed Billi, P.), pp. 65–87. Springer Netherlands, Dordrecht.
- Fleitmann, D., Burns, S.J., Pekala, M., Mangini, A., Al-Subary, A., Al-Aowah, M., Kramers, J. and Matter, A.** (2011) Holocene and Pleistocene pluvial periods in Yemen, southern Arabia. *Quat. Sci. Rev.*, **30**, 783–787.
- Foerster, V., Asrat, A., Bronk Ramsey, C., Brown, E.T., Chapot, M.S., Deino, A., Duesing, W., Grove, M., Hahn, A., Junginger, A., Kaboth-Bahr, S., Lane, C.S., Opitz, S., Noren, A., Roberts, H.M., Stockhecke, M., Tiedemann, R., Vidal, C.M., Vogelsang, R., Cohen, A.S., Lamb, H.F., Schaebitz, F. and Trauth, M.H.** (2022) Pleistocene climate variability in eastern Africa influenced hominin evolution. *Nat. Geosci.*, **15**, 805–811.
- Foubert, A., Kidane, T. and Atnafu, B.** (2018) Stepping stones towards a unique archive in the Danakil Basin: Afar Dallol Drilling - ONset of sedimentary processes in an active rift basin (ADD-ON). 20th EGU General Assembly, EGU2018, Proceedings from the conference held 4–13 April, 2018 in Vienna, Austria, 18894.
- Foubert, A., Keir, D., Atnafu, B., Kidane, T. and the ADD-ON Workshop Consortium** (2024) Workshop report ADD-ON: Afar Dallol Drilling - ONset of sedimentary processes in an active rift basin. *Sci. Drill.*, **33**, 207–218.
- Garcia-Veigas, J., Ort, F., Rosell, L., Ayora, C., Rouchy, J.-M. and Lugli, S.** (1995) The Messinian salt of the Mediterranean: geochemical study of the salt from the Central Sicily Basin and comparison with the Lorca Basin (Spain). *Bull. Soc. Géol. France*, **166**, 699–710.
- García-Veigas, J., Cendón, D.I., Gibert, L., Lowenstein, T.K. and Artiaga, D.** (2018) Geochemical indicators in Western Mediterranean Messinian evaporites: implications for the salinity crisis. *Mar. Geol.*, **403**, 197–214.
- Gauntlett, M., Stephenson, S.N., Kendall, J.-M., Ogden, C., Hammond, J.O.S., Hudson, T., Goitom, B. and Ogubazghi, G.** (2024) The dynamic crust of Northern Afar and Adjacent Rift Margins: new evidence from receiver function analysis in Eritrea and Ethiopia. *Geochem. Geophys. Geosyst.*, **25**, e2023GC011314.
- Gillespie, R., Street-perrott, F.A. and Switsur, R.** (1983) Post-glacial arid episodes in Ethiopia have implications for climate prediction. *Nature*, **306**, 680–683.
- Giordana, G., Thomas, R., Silvia, S., Berger, J.P., Dominik, F., Frank, P., Mahmoud, A.L.S. and Matter, A.** (2011) Faunal evidence of a holocene pluvial phase in southern Arabia with remarks on the morphological variability of *helenina anderseni*. *J. Foraminifer. Res.*, **41**, 248–259.
- Gramann, F.** (1971) Ostracoda aus Neogen und Quartär der Danakil-Senke (Nordost-Athiopien). *Beihefte zum Geologischen Jahrbuch*, **106**, 109–142.
- Grant, K.M., Rohling, E.J., Ramsey, C.B., Cheng, H., Edwards, R.L., Florindo, F., Heslop, D., Marra, F., Roberts, A.P., Tamisiea, M.E. and Williams, D.** (2014) Sea-level variability over five glacial cycles. *Nat. Commun.*, **5**, 5076.
- Hajdas, I.** (2008) Radiocarbon dating and its applications in Quaternary studies. *E&G Quat. Sci. J.*, **57**, 2–24.
- Hajdas, I., Ascough, P., Garnett, M.H., Fallon, S.J., Pearson, C.L., Quarta, G., Spalding, K.L., Yamaguchi, H. and Yoneda, M.** (2021) Radiocarbon dating. *Nat. Rev. Methods Primers*, **1**, 62.
- Hardie, L.A.** (1984) Evaporites; marine or non-marine? *Am. J. Sci.*, **284**, 193–240.
- Hardie, L.A.** (1990) The roles of rifting and hydrothermal CaCl₂ brines in the origin of potash evaporites: a hypothesis. *Am. J. Sci.*, **290**, 43–106.
- Hardie, L.A.** (1991) On the significance of evaporites. *Annu. Rev. Earth Planet. Sci.*, **19**, 131–169.
- Hardie, L.A., Lowenstein, T.K. and Spencer, R.J.** (1985) The problem of distinguishing between primary and secondary features in evaporites. *Sixth International Symposium on Salt*, **1**, 173–195.
- van Harten, D.** (2000) Variable nodding in *Cyprideis torosa* (Ostracoda, Crustacea): an overview, experimental results and a model from Catastrophe Theory. *Hydrobiologia*, **419**, 131–139.
- Harvie, C.E., Wear, J.H., Hardie, L.A. and Eugster, H.P.** (1980) Evaporation of seawater: calculated mineral sequences. *Science*, **208**, 498–500.
- Hassan, M., Faleide, J.I., Gabrielsen, R.H. and Tsikalas, F.** (2020) Carboniferous graben structures, evaporite accumulations and tectonic inversion in the southeastern Norwegian Barents Sea. *Mar. Pet. Geol.*, **112**, 104038.
- Hay, W.W., Migdisov, A., Balukhovskiy, A.N., Wold, C.N., Flögel, S. and Söding, E.** (2006) Evaporites and the salinity of the ocean during the Phanerozoic: IMPLICATIONS for climate, ocean circulation and life. *Palaeogeogr. Palaeoclimatol. Palaeoecol.*, **240**, 3–46.
- Herrmann, A.G.** (1972) Bromine distribution coefficients for halite precipitated from modern sea water under natural conditions. *Contrib. Mineral. Petrol.*, **37**, 249–252.
- Herrmann, A.G.** (1980) Bromide distribution between halite and NaCl-saturated seawater. *Chem. Geol.*, **28**, 171–177.
- Herrmann, A.G., Knake, D., Schneider, J. and Peters, H.** (1973) Geochemistry of modern seawater and brines from salt pans: main components and bromine distribution. *Contrib. Mineral. Petrol.*, **40**, 1–24.

- Holland, H.D.** (1984) *The Chemical Evolution of the Atmosphere and Oceans*. Princeton University Press, Princeton.
- Holser, W.T.** (1966) Bromide geochemistry of salt rocks. In: *Second Symposium on Salt, Northern Ohio Geological Society* (Ed Rau, J.L.), pp. 248–275. The Northern Ohio Geological Soc. Inc, Cleveland.
- Holser, W.T.** (1979) Chapter 9. Trace elements and isotopes in evaporites. In: *Reviews in Mineralogy 6: Marine Minerals* (Ed Burns, R.G.), pp. 295–346. *De Gruyter*, Berlin, Boston.
- Holser, W.T., Clement, G.P., Jansa, L.F. and Wade, J.A.** (1988) Evaporite deposits of the North Atlantic rift. *Dev. Geotectonics*, **22**, 525–556.
- Holwerda, U.G. and Hutchinson, R.W.** (1968) Potash-bearing evaporites in the Danakil Area, Ethiopia. *Econ. Geol.*, **2**, 124–150.
- Horton, B.P., Edwards, R.J. and Lloyd, J.M.** (1999) UK intertidal foraminiferal distributions: implications for sea-level studies. *Mar. Micropaleontol.*, **36**, 205–223.
- Hovland, M., Rueslatten, H. and Johnsen, H.K.** (2018a) Large salt accumulations as a consequence of hydrothermal processes associated with ‘Wilson cycles’: a review Part 1: towards a new understanding. *Mar. Pet. Geol.*, **92**, 987–1009.
- Hovland, M., Rueslatten, H. and Johnsen, H.K.** (2018b) Large salt accumulations as a consequence of hydrothermal processes associated with ‘Wilson cycles’: a review, Part 2: application of a new salt-forming model on selected cases. *Mar. Pet. Geol.*, **92**, 128–148.
- Hsü, K.J.** (1972) Origin of saline giants: a critical review after the discovery of the Mediterranean Evaporite. *Earth Sci. Rev.*, **8**, 371–396.
- Hübscher, C., Cartwright, J., Cypionka, H., DeLange, G.J., Robertson, A., Suc, J.-P. and Urai, J.L.** (2007) Global look at salt giants. *Eos*, **88**, 177–179.
- Hudec, M.R., Norton, I.O., Jackson, M.P.A. and Peel, F.J.** (2013) Jurassic evolution of the Gulf of Mexico salt basin. *Am. Assoc. Pet. Geol. Bull.*, **97**, 1683–1710.
- Hughes, G.W. and Beydoun, Z.R.** (1992) The Red Sea—Gulf of Aden: biostratigraphy, lithostratigraphy and palaeoenvironments. *J. Petrol. Geol.*, **15**, 135–156.
- Hurley, P.M.** (1966) K-Ar dating of sediments. In: *Potassium Argon Dating* (Eds Schaefer, O.A. and Zähringer, J.), pp. 134–151. *Springer*, Berlin, Heidelberg.
- Hurman, G.L., Keir, D., Bull, J.M., McNeill, L.C., Booth, A.D. and Bastow, I.D.** (2023) Quantitative analysis of faulting in the danakil depression rift of Afar: the importance of faulting in the final stages of magma-rich rifting. *Tectonics*, **42**, e2022TC007607.
- Hutchinson, R.W. and Engels, G.G.** (1970) Tectonic significance of regional geology and evaporite lithofacies in Northeastern Ethiopia. *Philos. Trans. R. Soc. A Math. Phys. Eng. Sci.*, **267**, 313–329.
- Hutchinson, R.W. and Engels, G.G.** (1972) Tectonic evolution in the Southern Red Sea and its possible significance to older rifted continental margins. *GSA Bull.*, **83**, 2989–3002.
- Jaramillo-Vogel, D., Foubert, A., Braga, J.C., Schaegis, J.-C., Atnafu, B., Grobety, B. and Kidane, T.** (2019) Pleistocene sea-floor fibrous crusts and spherulites in the Danakil Depression (Afar, Ethiopia). *Sedimentology*, **66**, 480–512.
- Jaramillo-Vogel, D., Braga, J.C., Negga, H.A., Vennemann, T., De Boever, E., Schaegis, J.-C., Rime, V., Atnafu, B., Kidane, T. and Foubert, A.** (2023) Pleistocene aragonite crust diagenesis mimics microbialite fabrics (Danakil Depression, Ethiopia). *Sed. Geol.*, **446**, 106341.
- Johnsen, H.K., Rueslatten, H.G. and Hovland, M.T.** (2021) The “Global Salt Cycle”: Formation of Giant Salt Accumulations, a Result of Subduction, Mantle Upwelling, and Rifting. [Preprint]. *Preprints (Basel)*, 2021070377.
- Karakaya, M.Ç., Bozdağ, A., Ercan, H.Ü., Karakaya, N. and Delikan, A.** (2019) Origin of Miocene halite from Tuz Gölü basin in Central Anatolia, Turkey: evidences from the pure halite and fluid inclusion geochemistry. *J. Geochem. Explor.*, **202**, 1–12.
- Kebede, S., Travi, Y., Asrat, A., Alemayehu, T., Ayenew, T. and Tessema, Z.** (2008) Groundwater origin and flow along selected transects in Ethiopian rift volcanic aquifers. *Hydrogeol. J.*, **16**, 55–73.
- Keir, D., Bastow, I.D., Pagli, C. and Chambers, E.L.** (2013) The development of extension and magmatism in the Red Sea rift of Afar. *Tectonophysics*, **607**, 98–114.
- Kirkham, C., Bertoni, C., Cartwright, J., Lensky, N.G., Sirota, I., Rodriguez, K. and Hodgson, N.** (2020) The demise of a ‘salt giant’ driven by uplift and thermal dissolution. *Earth Planet. Sci. Lett.*, **531**, 115933.
- Kirkland, D.W., Denison, R.E. and Dean, W.E.** (2000) Parent brine of the castile evaporites (Upper Permian), Texas and New Mexico. *J. Sed. Res.*, **70**, 749–761.
- Kiro, Y., Goldstein, S.L., Lazar, B. and Stein, M.** (2016) Environmental implications of salt facies in the Dead Sea. *Geol. Soc. Am. Bull.*, **128**, 824–841.
- Konstantinou, A., Karner, G.D., Kneller, E. and Gombosi, D.** (2023) Salt deposition in ultradeep brine settings by dynamic inflow and evaporation. *Bulletin*, **107**, 2023–2052.
- Kotopoulou, E., Delgado Huertas, A., Garcia-Ruiz, J.M., Dominguez-Vera, J.M., Lopez-Garcia, J.M., Guerra-Tschuschke, I. and Rull, F.** (2019) A polyextreme hydrothermal system controlled by Iron: The case of dallol at the Afar Triangle. *ACS Earth Space Chem.*, **3**, 90–99.
- Krijgsman, W. and Meijer, P.T.** (2008) Depositional environments of the Mediterranean “Lower Evaporites” of the Messinian salinity crisis: constraints from quantitative analyses. *Mar. Geol.*, **253**, 73–81.
- Kuhn, R.** (1968) Geochemistry of the german potash deposits. *Spec. Pap. Geol. Soc. Am.*, **88**, 427–504.
- Kühn, R. and Hsü, K.J.** (1974) Bromine Content of Mediterranean Halite. *Geology*, **2**, 213.
- Kukla, P.A., Strozyk, F. and Mohriak, W.U.** (2018) South Atlantic salt basins – witnesses of complex passive margin evolution. *Gondwana Res.*, **53**, 41–57.
- Lalou, C., van Nguyen, H., Faure, H. and Moreira, L.** (1970) Datation par la méthode Uranium-Thorium des hauts niveaux de coraux de la dépression de l’Afar (Ethiopie). *Rev. Géogr. Phys. Géol. Dynam.*, **12**, 3–8.
- Lamb, H.F., Bates, C.R., Bryant, C.L., Davies, S.J., Huws, D.G., Marshall, M.H. and Roberts, H.M.** (2018) 150000-year palaeoclimate record from northern Ethiopia supports early, multiple dispersals of modern humans from Africa. *Sci. Rep.*, **8**, 1077.
- de Lange, G.J. and Krijgsman, W.** (2010) Messinian salinity crisis: a novel unifying shallow gypsum/deep dolomite formation mechanism. *Mar. Geol.*, **275**, 273–277.
- Le Gall, B., Leleu, S., Pik, R., Jourdan, F., Chazot, G., Ayalew, D., Yirgu, G., Cloquet, C. and Chauvet, F.** (2018) The Red Beds series in the Ertale segment, North Afar. Evidence for a 6 Ma-old post-rift basin prior to continental rifting. *Tectonophysics*, **747–748**, 373–389.
- Lensky, N.G., Dvorkin, Y., Lyakhovskiy, V., Gertman, I. and Gavrieli, I.** (2005) Water, salt, and energy balances of the Dead Sea. *Water Resour. Res.*, **41**, 1–13.

- Li, J., Lowenstein, T.K., Brown, C.B., Ku, T.L. and Luo, S. (1996) A 100 ka record of water tables and paleoclimates from salt cores, Death Valley, California. *Palaeogeogr. Palaeoclimatol. Palaeoecol.*, **123**, 179–203.
- Logan, B.W. (1987) *The MacLeod Evaporite Basin, Western Australia Holocene Environments, Sediments and Geological Evolution*, Vol. **44**, p. 140. American Association of Petroleum Geologists, Tulsa, Oklahoma.
- López-García, J.M., Moreira, D., Benzerara, K., Grunewald, O. and López-García, P. (2020) Origin and Evolution of the Halo-Volcanic Complex of Dallol: Proto-Volcanism in Northern Afar (Ethiopia). *Front. Earth Sci.*, **7**, 351.
- Lowenstein, T.K. and Hardie, L.A. (1985) Criteria for the recognition of salt-pan evaporites. *Sedimentology*, **32**, 627–644.
- Lugli, S., Manzi, V., Roveri, M. and Schreiber, C.B. (2010) The Primary Lower Gypsum in the Mediterranean: a new facies interpretation for the first stage of the Messinian salinity crisis. *Palaeogeogr. Palaeoclimatol. Palaeoecol.*, **297**, 83–99.
- Lugli, S., Manzi, V., Roveri, M. and Schreiber, B.C. (2015) The deep record of the Messinian salinity crisis: evidence of a non-desiccated Mediterranean Sea. *Palaeogeogr. Palaeoclimatol. Palaeoecol.*, **433**, 201–218.
- Makris, J. and Ginzburg, A. (1987) The Afar depression: transition between continental rifting and sea-floor spreading. *Tectonophysics*, **141**, 199–214.
- Manzi, V., Roveri, M., Gennari, R., Bertini, A., Biffi, U., Giunta, S., Iaccarino, S.M., Lanci, L., Lugli, S., Negri, A., Riva, A., Rossi, M.E. and Taviani, M. (2007) The deep-water counterpart of the Messinian Lower Evaporites in the Apennine foredeep: the Fananello section (Northern Apennines, Italy). *Palaeogeogr. Palaeoclimatol. Palaeoecol.*, **251**, 470–499.
- Manzi, V., Lugli, S., Roveri, M., Schreiber, B.C. and Gennari, R. (2011) The Messinian “Calcare di Base” (Sicily, Italy) revisited. *Geol. Soc. Am. Bull.*, **123**, 347–370.
- Manzi, V., Gennari, R., Lugli, S., Roveri, M., Scafetta, N. and Schreiber, B.C. (2012) High-frequency cyclicity in the Mediterranean Messinian evaporites: evidence for solar-lunar climate forcing. *J. Sed. Res.*, **82**, 991–1005.
- Manzi, V., Gennari, R., Lugli, S., Persico, D., Reghizzi, M., Roveri, M., Schreiber, B.C., Calvo, R., Gavrieli, I. and Gvirtzman, Z. (2018) The onset of the Messinian salinity crisis in the deep Eastern Mediterranean basin. *Terra Nova*, **30**, 189–198.
- Master, S. (2016) Gaet’ale- a reactivated thermal spring and potential tourist hazard in the Asale salt flats, Danakil Depression, Ethiopia. *J. Appl. Volcanol.*, **5**, 1.
- McCaffrey, M.A., Lazar, B. and Holland, H.D. (1987) The evaporation path of seawater and the coprecipitation of Br- and K+ with Halite. *SEPM J. Sed. Res.*, **57**, 928–937.
- McClusky, S., Reilinger, R., Ogubazghi, G., Amleson, A., Healeb, B., Vernant, P., Sholan, J., Fisseha, S., Asfaw, L., Bendick, R. and Kogan, L. (2010) Kinematics of the southern Red Sea-Afar Triple Junction and implications for plate dynamics. *Geophys. Res. Lett.*, **37**, 1–5.
- Meaza, H., Hermans, L., Nyssen, J., Frankl, A., Zenebe, A., Demissie, B., Asfaha, T.G., Van Eetvelde, V., Deckers, J. and Poesen, J. (2019) Spatial and temporal patterns of water salinity in the marginal grabens of Ethiopia’s Danakil depression. *Land Degrad. Dev.*, **30**, 1407–1422.
- Meijer, P.T. (2006) A box model of the blocked-outflow scenario for the Messinian Salinity Crisis. *Earth Planet. Sci. Lett.*, **248**, 486–494.
- Meilijon, A., Hilgen, F., Sepúlveda, J., Steinberg, J., Fairbank, V., Flecker, R., Waldmann, N.D., Spaulding, S.A., Bialik, O.M., Boudinot, F.G., Illner, P. and Makovsky, Y. (2019) Chronology with a pinch of salt: integrated stratigraphy of Messinian evaporites in the deep Eastern Mediterranean reveals long-lasting halite deposition during Atlantic connectivity. *Earth Sci. Rev.*, **194**, 374–398.
- Mohr, P. and Zanettin, B. (1988) The Ethiopian flood basalt province. In: *Continental Flood Basalts* (Ed Macdougall, J.D.), pp. 63–110. Springer, Dordrecht.
- Mojtahid, M., Geslin, E., Coynel, A., Gorse, L., Vella, C., Davranche, A., Zozzolo, L., Blanchet, L., Bénétteau, E. and Maillet, G. (2016) Spatial distribution of living (Rose Bengal stained) benthic foraminifera in the Loire estuary (western France). *J. Sea Res.*, **118**, 1–16.
- Montaron, B.A. (2016) A forward model of messinian salt deposition in the Mediterranean Sea: key results and implications for basin modeling. In: *EAGE/SPE Subsalt Imaging Workshop, European Association of Geoscientists & Engineers*, pp. 1–5.
- Montaron, B. and Tapponnier, P. (2010) A quantitative model for salt deposition in actively spreading basins. *Search Discovery*, 30117.
- Morel, M. and Serneels, V. (2021) Interpreting the chemical variability of iron smelting slag: a case study from Northeastern Madagascar. *Minerals*, **11**, 900.
- Moretto, R. (1988) Observations on the incorporation of trace elements in halite of Oligocene salt beds, Bourg-en-Bresse Basin, France. *Geochim. Cosmochim. Acta*, **52**, 2809–2814.
- Munzinger, W. (1869) Narrative of a Journey through the Afar Country. *J. R. Geogr. Soc. Lond.*, **39**, 188–232.
- Nahnybida, T., Gleeson, S.A., Rusk, B.G. and Wassenaar, L.I. (2009) Cl/Br ratios and stable chlorine isotope analysis of magmatic-hydrothermal fluid inclusions from Butte, Montana and Bingham Canyon, Utah. *Miner. Depos.*, **44**, 837–848.
- Negga, H. (2024) Characterization of marginal sediments in active rift basins : case study of the Danakil depression (Afar). PhD Thesis, University of Fribourg, 327 pp.
- Nicholson, S.L., Pike, A.W.G., Hosfield, R., Roberts, N., Sahy, D., Woodhead, J., Cheng, H., Edwards, R.L., Affolter, S., Leuenberger, M., Burns, S.J., Matter, A. and Fleitmann, D. (2020) Pluvial periods in Southern Arabia over the last 1.1 million-years. *Quat. Sci. Rev.*, **229**, 106112.
- Nitsche, C., Schreurs, G. and Serneels, V. (2023) The enigmatic softstone vessels of Northern Madagascar: petrological investigations of a medieval quarry. *J. Field Archaeol.*, **48**, 55–72.
- Nobile, A., Pagli, C., Keir, D., Wright, T.J., Ayele, A., Ruch, J. and Acocella, V. (2012) Dike-fault interaction during the 2004 Dallol intrusion at the northern edge of the Erta Ale Ridge (Afar, Ethiopia). *Geophys. Res. Lett.*, **39**, L19305.
- Orszag-Sperber, F., Harwood, G., Kendall, A. and Purser, B.H. (1998) A review of the evaporites of the Red Sea - Gulf of Suez rift. In: *Sedimentation and Tectonics in Rift Basins: Red Sea - Gulf of Aden* (Eds Purser, B.H. and Bosence, D.W.), pp. 409–426. Chapman & Hall, London.
- Otálora, F., Palero, F., Papaslioti, E.-M. and García-Ruiz, J.M. (2022) Mineralochemical mechanism for the formation of Salt Volcanoes: the case of Mount Dallol

- (Afar Triangle, Ethiopia). *ACS Earth Space Chem.*, **6**, 2767–2778.
- Patterson, R.T., McKillop, W.B., Kroker, S., Nielsen, E. and Reinhardt, E.G.** (1997) Evidence for rapid avian-mediated foraminiferal colonization of Lake Winnipegosis, Manitoba, during the Holocene Hypsithermal. *J. Paleolimnol.*, **18**, 131–143.
- Peel, F.** (2019) The Louann Salt of the Gulf of Mexico: how long does it take to deposit a giant salt deposit? In: *American Association of Petroleum Geologists Annual Convention and Exhibition, San Antonio, Texas.*
- Pérez, E. and Chebude, Y.** (2017) Chemical analysis of Gaet'ale, a hypersaline pond in Danakil Depression (Ethiopia): new record for the Most Saline Water Body on Earth. *Aquat. Geochem.*, **23**, 109–117.
- Perthuisot, J.P.** (1971) Recent Polyhalite from Sebkhah el Melah (Tunisia). *Nat. Phys. Sci.*, **232**, 186–187.
- Pichat, A., Delhaye-Prat, V., Guiraud, M., Gindre-Chanu, L. and Gaucher, E.C.** (2024) Palaeogeography and tectono-stratigraphic evolution of the Aptian Ezanga-Loémé evaporites along the proximal domain of the south Gabon-Congo-Cabinda margin. *Basin Res.*, **36**, e12893.
- Pint, A., Engel, M., Melzer, S., Frenzel, P., Plessen, B. and Brückner, H.** (2017) How to discriminate athalassic and marginal marine microfaunas: Foraminifera and other fossils from an early holocene continental lake in northern Saudi Arabia. *J. Foraminifer. Res.*, **47**, 175–187.
- Pudovskis, M., Selley, D., Espinosa, S., Pettit, W. and Molloy, R.** (2012) Danakil Potash Project, technical report - September 2008 - September 2012 - BHP Billiton Minerals Exploration. 55 pp.
- Qin, Z., Tang, C., Liu, L., Chen, T. and Gong, B.** (2023) Large evaporite provinces: warming from above or heating from below? *Innovation Geosci.*, **1**, 1–2.
- Ralph M. Parsons Company.** (1967) Ground-Water Conditions at Dallol, Ethiopia. Internal Report 25 pp.
- Rauche, H. and van der Klauw, S.** (2011) Resource Report for the Danakil Potash Deposit, Afar State/Ethiopia - Technical Report. 117 pp.
- Raup, O.B. and Hite, R.J.** (1978) Bromine distribution in marine Halite rocks. In: *Marine Evaporites* (Eds Dean, W.E. and Schreiber, C.), Vol. **4**, pp. 105–123. SEMP Short Course.
- Raup, O.B. and Hite, R.J.** (1996) Bromine geochemistry of chloride rocks of the middle Pennsylvanian Paradox Formation of the Hermosa Group, Paradox Basin, Utah and Colorado. *U.S. Geological Survey Bulletin*, 2000–M, 117 pp.
- Reimer, P.J., Austin, W.E.N., Bard, E., Bayliss, A., Blackwell, P.G., Bronk Ramsey, C., Butzin, M., Cheng, H., Edwards, R.L., Friedrich, M., Grootes, P.M., Guilderson, T.P., Hajdas, I., Heaton, T.J., Hogg, A.G., Hughen, K.A., Kromer, B., Manning, S.W., Muscheler, R., Palmer, J.G., Pearson, C., Van Der Plicht, J., Reimer, R.W., Richards, D.A., Scott, E.M., Southon, J.R., Turney, C.S.M., Wacker, L., Adolphi, F., Büntgen, U., Capano, M., Fahrni, S.M., Fogtmann-Schulz, A., Friedrich, R., Köhler, P., Kudsk, S., Miyake, F., Olsen, J., Reinig, F., Sakamoto, M., Sookdeo, A. and Talamo, S.** (2020) The IntCal20 Northern Hemisphere Radiocarbon Age Calibration Curve (0–55 cal kBP). *Radiocarbon*, **62**, 725–757.
- Riedel, F., Kossler, A., Tarasov, P. and Wünnemann, B.** (2011) A study on Holocene foraminifera from the Aral Sea and West Siberian lakes and its implication for migration pathways. *Quatern. Int.*, **229**, 105–111.
- Rime, V., Foubert, A., Atnafu, B. and Kidane, T.** (2022) Geological map of the Afar depression. *Zenodo*. <https://doi.org/10.5281/zenodo.7351643>
- Rime, V., Foubert, A., Ruch, J. and Kidane, T.** (2023) Tectonostratigraphic evolution and significance of the Afar Depression. *Earth Sci. Rev.*, **244**, 104519.
- Rodier, J. and Serneels, V.** (2023) Geochemical link between slag inclusion and hammer scale, a potential new tool to better understand the iron supply of an archaeological workshop. *Metallogr. Microstruct. Anal.*, **12**, 312–326.
- Rodriguez, C.R., Jackson, C.A.L., Rotevatn, A., Bell, R.E. and Francis, M.** (2018) Dual tectonic-climatic controls on salt giant deposition in the Santos Basin, offshore Brazil. *Geosphere*, **14**, 215–242.
- Rosenberg, T.M., Preusser, F., Fleitmann, D., Schwalb, A., Penkman, K., Schmid, T.W., Al-Shanti, M.A., Kadi, K. and Matter, A.** (2011) Humid periods in southern Arabia: Windows of opportunity for modern human dispersal. *Geology*, **39**, 1115–1118.
- Roveri, M., Flecker, R., Krijgsman, W., Lofi, J., Lugli, S., Manzi, V., Sierro, F.J., Bertini, A., Camerlenghi, A., De Lange, G., Govers, R., Hilgen, F.J., Hübscher, C., Meijer, P.T. and Stoica, M.** (2014) The Messinian Salinity Crisis: past and future of a great challenge for marine sciences. *Mar. Geol.*, **352**, 25–58.
- Ryan, W.B.F.** (2009) Decoding the Mediterranean salinity crisis. *Sedimentology*, **56**, 95–136.
- Salvany, J.M., García-Veigas, J. and Orti, F.** (2007) Glauberite-halite association of the Zaragoza Gypsum Formation (Lower Miocene, Ebro Basin, NE Spain). *Sedimentology*, **54**, 443–467.
- Schaebitz, F., Asrat, A., Lamb, H.F., Cohen, A.S., Foerster, V., Duesing, W., Kaboth-Bahr, S., Opitz, S., Viehberg, F.A., Vogelsang, R., Dean, J., Leng, M.J., Junginger, A., Ramsey, C.B., Chapot, M.S., Deino, A., Lane, C.S., Roberts, H.M., Vidal, C., Tiedemann, R. and Trauth, M.H.** (2021) Hydroclimate changes in eastern Africa over the past 200 000 years may have influenced early human dispersal. *Commun. Earth Environ.*, **2**, 123.
- Schlöder, Z. and Urai, J.L.** (2005) Microstructural evolution of deformation-modified primary halite from the Middle Triassic Röt Formation at Hengelo, The Netherlands. *Int. J. Earth Sci.*, **94**, 941–955.
- Schreiber, B.C. and El Tabakh, M.** (2000) Deposition and early alteration of evaporites. *Sedimentology*, **47**, 215–238.
- Schubel, K.A. and Lowenstein, T.K.** (1997) Criteria for the recognition of shallow-perennial-saline-lake halites based on Recent sediments from the Qaidam Basin, western China. *J. Sed. Res.*, **67**, 74–87.
- Scribano, V., Carbone, S., Manuella, F.C., Hovland, M., Rueslätten, H. and Johnsen, H.-K.** (2017) Origin of salt giants in abyssal serpentinite systems. *Int. J. Earth Sci.*, **106**, 2595–2608.
- Shearman, D.J.** (1970) Recent Halite rock, Baja California, Mexico. *Trans. Inst. Mining Metall. A Mining Technol.*, **B79**, 127–136.
- Shields, G.A. and Mills, B.J.W.** (2020) Evaporite weathering and deposition as a long-term climate forcing mechanism. *Geology*, **49**, 299–303.
- Simon, D. and Meijer, P.** (2015) Dimensions of the Atlantic–Mediterranean connection that caused the Messinian Salinity Crisis. *Mar. Geol.*, **364**, 53–64.
- Simon, D. and Meijer, P.T.** (2017) Salinity stratification of the Mediterranean Sea during the Messinian crisis: A

- first model analysis. *Earth Planet. Sci. Lett.*, **479**, 366–376.
- Sirota, I., Enzel, Y. and Lensky, N.G.** (2017) Temperature seasonality control on modern halite layers in the Dead Sea: in situ observations. *Geol. Soc. Am. Bull.*, **129**, B31661.1.
- Sirota, I., Enzel, Y. and Lensky, N.G.** (2018) Halite focusing and amplification of salt layer thickness: from the Dead Sea to deep hypersaline basins. *Geology*, **46**, 851–854.
- Sirota, I., Enzel, Y., Mor, Z., Ben Moshe, L., Eyal, H., Lowenstein, T.K. and Lensky, N.G.** (2021) Sedimentology and stratigraphy of a modern halite sequence formed under Dead Sea level fall. *Sedimentology*, **68**, 1069–1090.
- Smith, J.E. and Santamarina, J.C.** (2022) Red sea evaporites: formation, creep and dissolution. *Earth Sci. Rev.*, **232**, 115.
- Soto, J.I., Flinch, J.F. and Tari, G.** (2017) Permo-triassic basins and tectonics in Europe, North Africa and the Atlantic Margins. In: *Permo-Triassic Salt Provinces of Europe, North Africa and the Atlantic Margins* (Eds Soto, J.I., Flinch, J.F. and Tari, G.), pp. 3–41. Elsevier, Amsterdam.
- Spencer, R.J.** (2000) Sulfate minerals in evaporite deposits. *Rev. Mineral. Geochem.*, **40**, 173–192.
- Synal, H.A., Stocker, M. and Suter, M.** (2007) MICADAS: a new compact radiocarbon AMS system. *Nucl. Inst. Methods Phys. Res. B*, **259**, 7–13.
- Taberner, C., Cendón, D.I., Pueyo, J.J. and Ayora, C.** (2000) The use of environmental markers to distinguish marine vs. continental deposition and to quantify the significance of recycling in evaporite basins. *Sed. Geol.*, **137**, 213–240.
- Talbot, C.J.** (2008) Hydrothermal salt—but how much? *Mar. Pet. Geol.*, **25**, 191–202.
- Tazieff, H.** (1969) Potash-bearing evaporites; danakil area [discussion]. *Econ. Geol.*, **64**, 228–229.
- Tierney, J.E., deMenocal, P.B. and Zander, P.D.** (2017) A climatic context for the out-of-Africa migration. *Geology*, **45**, 1023–1026.
- Topper, R.P.M. and Meijer, P.T.** (2013) A modeling perspective on spatial and temporal variations in Messinian evaporite deposits. *Mar. Geol.*, **336**, 44–60.
- Tzevahirtzian, A., Caruso, A., Scopelliti, G., Baudin, F. and Blanc-Valleron, M.-M.** (2022) Onset of the Messinian Salinity Crisis: sedimentological, petrographical and geochemical characterization of the pre-salt sediments from a new core (Caltanissetta Basin, Sicily). *Mar. Pet. Geol.*, **141**, 686.
- Ukstins, I.A., Renne, P.R., Wolfenden, E., Baker, J., Ayalew, D. and Menzies, M.** (2002) Matching conjugate volcanic rifted margins: 40Ar/39Ar chrono-stratigraphy of pre- and syn-rift bimodal flood volcanism in Ethiopia and Yemen. *Earth Planet. Sci. Lett.*, **198**, 289–306.
- Usiglio, M.J.** (1849) Études sur la composition de l'eau de la Méditerranée et sur l'exploitation des sels qu'elle contient. *Ann. Chimie Phys.*, **3**, 172–191.
- Valyashko, M.G.** (1956) Geochemistry of bromine in the processes of salt deposition and the use of the bromine content as a genetic and prospecting criterion. *Geochemistry*, **6**, 570–589.
- Van Krevelen, D.W.** (1993) *Coal: Typology-Physics-Chemistry-Constitution*, 3rd edn. Elsevier, Amsterdam.
- Varet, J.** (2018) *Geology of Afar (East Africa)*. Springer, Cham, 336 pp.
- Vasconcelos, C. and Mckenzie, J.A.** (1997) Microbial mediation of modern dolomite precipitation and diagenesis under anoxic conditions (Lagoa Vermelha, Rio de Janeiro, Brazil). *J. Sed. Res.*, **67**, 378–390.
- Vengosh, A., Helvacı, C. and Karamanderesi, İ.H.** (2002) Geochemical constraints for the origin of thermal waters from western Turkey. *Appl. Geochem.*, **17**, 163–183.
- Viltres, R., Jónsson, S., Ruch, J., Doubre, C., Reilinger, R., Floyd, M. and Ogubazghi, G.** (2020) Kinematics and deformation of the southern Red Sea region from GPS observations. *Geophys. J. Int.*, **221**, 2143–2154.
- Wang, T., Gao, S.S., Yang, Q. and Liu, K.H.** (2021) Crustal structure beneath the Ethiopian Plateau and adjacent areas from receiver functions: implications for partial melting and magmatic underplating. *Tectonophysics*, **809**, 857.
- Warren, J.K.** (2010) Evaporites through time: tectonic, climatic and eustatic controls in marine and nonmarine deposits. *Earth Sci. Rev.*, **98**, 217–268.
- Warren, J.K.** (2016) *Evaporites: A Geological Compendium*, p. 1822. Springer, Cham, Heidelberg, New York, Dordrecht, London.
- Wennrich, V., Meng, S. and Schmiedl, G.** (2007) Foraminifers from Holocene sediments of two inland brackish lakes in central Germany. *J. Foraminifer. Res.*, **37**, 318–326.
- Wilgus, C.K. and Holser, W.T.** (1984) Marine and nonmarine salts of Western Interior, United States. *Am. Assoc. Pet. Geol. Bull.*, **68**, 765–767.
- Wouters, K.** (2002) On the distribution of *Cyprideis torosa* (Jones) (Crustacea, Ostracoda) in Africa, with the discussion of a new record from the Seychelles. *Bull. l'Inst. R. Sci. Nat. Belgique Biol.*, **72**, 131–140.

Manuscript received 21 July 2023; revision accepted 10 September 2024

Supporting Information

Additional information may be found in the online version of this article:

Figure S1. Detail of the potash interval of Core A.

Figure S2. Lithological column of Core B.

Figure S3. Results of radiocarbon dating on wood and shell fragments.

Figure S4. Scanning electron microscopy (SEM) images of foraminifera found in Core A.

Figure S5. Scanning electron microscopy (SEM) images of foraminifera found in Core A.

Figure S6. Scanning electron microscopy (SEM) images of ostracods found in Core A.

Data S1. Description of bromide measurements of halite samples using ion chromatography and calibration of X-ray fluorescence (XRF) data.

Table S1. List of samples, depth of units and results of laboratory analysis [X-ray fluorescence (XRF), ion chromatography (IC), X-ray diffraction (XRD), Rock-Eval® and radiocarbon] for Core A.